CJC Chinese Journal of Chemistry 中国化学 · An International Journal

For submission: https://mc.manuscriptcentral.com/cjoc
For published articles: https://onlinelibrary.wiley.com/journal/16147065

Recent Advances

Cite this paper: *Chin. J. Chem.* **2022**, *40*, 989—1004. **DOI: 10.1002/cjoc.202100777**

# Polymorph Structures, Rich Physical Properties and Potential Applications of Two-Dimensional $MoTe_2$, $WTe_2$ and Their Alloys†

Rui Zhou,[a,b] Juanxia Wu,[a] Yuansha Chen,*[,c] and Liming Xie*[,a,b]

[a] *CAS Key Laboratory of Standardization and Measurement for Nanotechnology, National Center for Nanoscience and Technology, Beijing 100190, China*
[b] *University of Chinese Academy of Sciences, Beijing 100049, China*
[c] *Beijing National Laboratory for Condensed Matter Physics & Institute of Physics, Chinese Academy of Sciences, Beijing 100190, China*

## Comprehensive Summary

2D $MoTe_2$, $WTe_2$ and their alloys have received intensive research interest because of their unique properties arising from the polymorph structures, chiral anomaly, strong spin-orbit coupling, and so on. In this review, we have summarized recent advances of 2D $MoTe_2$, $WTe_2$ and their alloys from the materials perspective with special focus on the synthesis, electrical and magnetic properties. The polymorph structures of $MoTe_2$, $WTe_2$ and their alloys are presented first and then the preparation methods have been discussed, including mechanical exfoliation, metal-organic chemical vapor deposition (MOCVD), molecular beam epitaxy (MBE), chemical vapor deposition (CVD) and solution-phase method. After that, fascinating physical properties arising from the large spin–orbit coupling and non-trivial band structures have been summarized, including phase transition, optoelectrical properties, Weyl semimetal state, superconducting and ferromagnetism. At last, potential device applications of $MoTe_2$, $WTe_2$ and their alloys are reviewed, including field-effect transistors (FETs), memory devices, spin-to-charge conversion, solar cells, and so on.

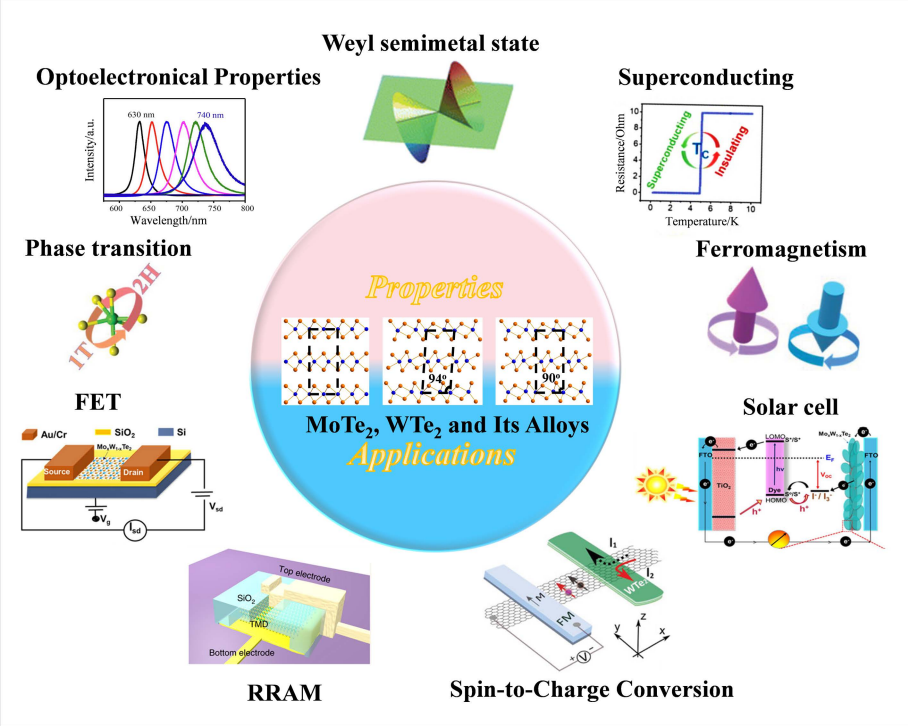


## Keywords

2D materials | Transition metal tellurides | Alloys | Crystal growth | Electronic structure

*E-mail: xielm@nanoctr.cn; yschen@iphy.ac.cn
† Dedicate to the Special Issue of 2D Materials.

View HTML Article

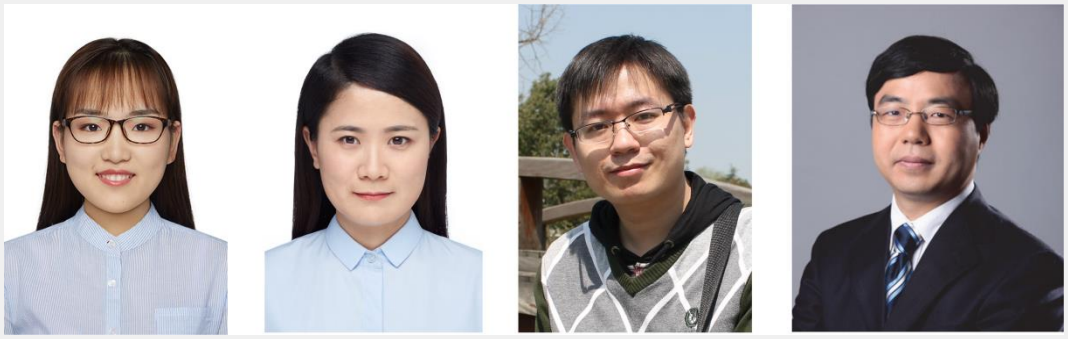

**Left to Right:** Rui Zhou, Juanxia Wu, Yuansha Chen, Liming Xie

Rui Zhou received her B. S. degree in Qingdao University of Science and Technology in 2018. She is a Ph.D. student at UCAS under the supervision of Prof. L. Xie. Her research interest is on the synthesis of 2D TMDs.

Dr. Juanxia Wu received her Ph.D. degree from Peking University in 2015, and also did her postdoctoral research at Peking University from 2015–2017. She joined NCNST as an assistant professor in 2018. Her research interest is Raman spectroscopy of low dimensional materials.

Dr. Yuansha Chen received his Ph.D. degree from Peking University in 2009 and also did his postdoctoral research at Peking University from 2009–2011. He joined the Institute of Physics at Chinese Academy of Sciences as an associate professor in 2011. His current research is on the quantum order regulation in strongly correlated oxide systems and magnetic properties of low dimensional materials.

Dr. Liming Xie received his Ph.D. degree from Peking University in 2009 and went to MIT as a visiting student in 2007–2008. He did his postdoctoral research at Stanford University in 2009–2012 and joined NCNST as a professor in 2012. His research interest is synthesis, devices and applications of 2D materials.

## Contents



## 1. Introduction

Two-dimensional (2D) materials, including graphene,[1] hexagonal boron nitride,[2] transition metal chalcogenides (TMCs),[3-4] black phosphorus,[5] are promising for a variety of potential applications in electronics, photoelectronics,[6-7] flexible electronics,[8] solar cells,[9] and so on. Among these 2D materials, TMCs have attracted extensive attention because of the large family of materials with diverse chemical and physical properties.[10-15]

Group VIB transition metal tellurides, *i.e.*, $MoTe_2$ and $WTe_2$, are a special sub-family of 2D TMCs because of the diverse crystal structures and intriguing physical properties,[16-17] arising from polymorph structures, chiral anomaly, strong spin-orbit coupling, and so on. For example, $WTe_2$ has large non-saturating magnetoresistance, which is promising for spintronic devices and magnetic memory.[18-21] $T_d$-$MoTe_2$ and $T_d$-$WTe_2$ atomic layers are type-II Weyl semimetals,[22-23] which are appealing for spin Hall effect devices.[24-25] Alloying of 2D $MoTe_2$ and $WTe_2$ can fine tuning these physical properties or even yield new properties. For example, Weyl semimetal and superconducting states are observed in $Mo_xW_{1-x}Te_2$ with different composites.[26] By Cr-doping, ferromagnetism emerges in $MoTe_2$ and $WTe_2$.[27-28]

In this review, we have reviewed the preparation, properties, and device applications of 2D $MoTe_2$, $WTe_2$ and their alloys (Figure 1). This review begins with the polymorph structures of $MoTe_2$ and $WTe_2$ and the phase diagram of Mo-W-Te-Se. Then the preparation methods for 2D $MoTe_2$, $WTe_2$ and the alloys are discussed, which include mechanical exfoliation, MOCVD, MBE, CVD and solution-phase method. Afterward, the properties of 2D $MoTe_2$, $WTe_2$ and the alloys are reviewed, including structural phase transition, optoelectronical properties, Weyl semimetal state, superconducting and ferromagnetism. At last, device applications of 2D $MoTe_2$, $WTe_2$ and the alloys are reviewed, including the field-effect transistors (FETs), memory devices, spin-to-charge conversion, solar cells and so on.

## 2. Crystal Structure and Phase Diagram

$MoTe_2$ and $WTe_2$ have three phases: 2H, 1T' and $T_d$. H or T refers to hexagonal or trigonal coordination of metal atoms by the Te atoms, respectively. In the 2H phase (point group $D_{3h}$), the Mo/W atoms have a trigonal-prismatic coordination by six Te atoms and layer-layer stacking is AB stacking (Figures 2A, D). While in 1T' and $T_d$ phases, distorted octahedral coordination is formed and the layer-layer stacking is AA stacking (Figures 2B, C).[29] The difference between 1T' and $T_d$ phase is the three-dimensional arrangement (Figures 2E, F), presenting the monoclinic (94°) and the orthorhombic (90°) arrangement, respectively.[30-31]

Figure 2G shows a partial phase diagram of M-W-Te-Se. At room temperature, the thermodynamic stable phase for $WTe_2$ is $T_d$ phase. Above 600 K, the thermodynamic stable phase of $WTe_2$ changes to 1T' phase.

As increase Se doping of $MoTe_2$, the stable phase of $MoSe_{2x}Te_{2-2x}$ changes from $T_d$ phase to 1T' phase at $x$ = 0.4, then to 2H phase at $x$ = 0.5. And when the temperature is lower than 3.6 K, superconducting phase appears in $T_d$ phase of $MoSe_{2x}Te_{2-2x}$ with $x$ < 0.5.

  

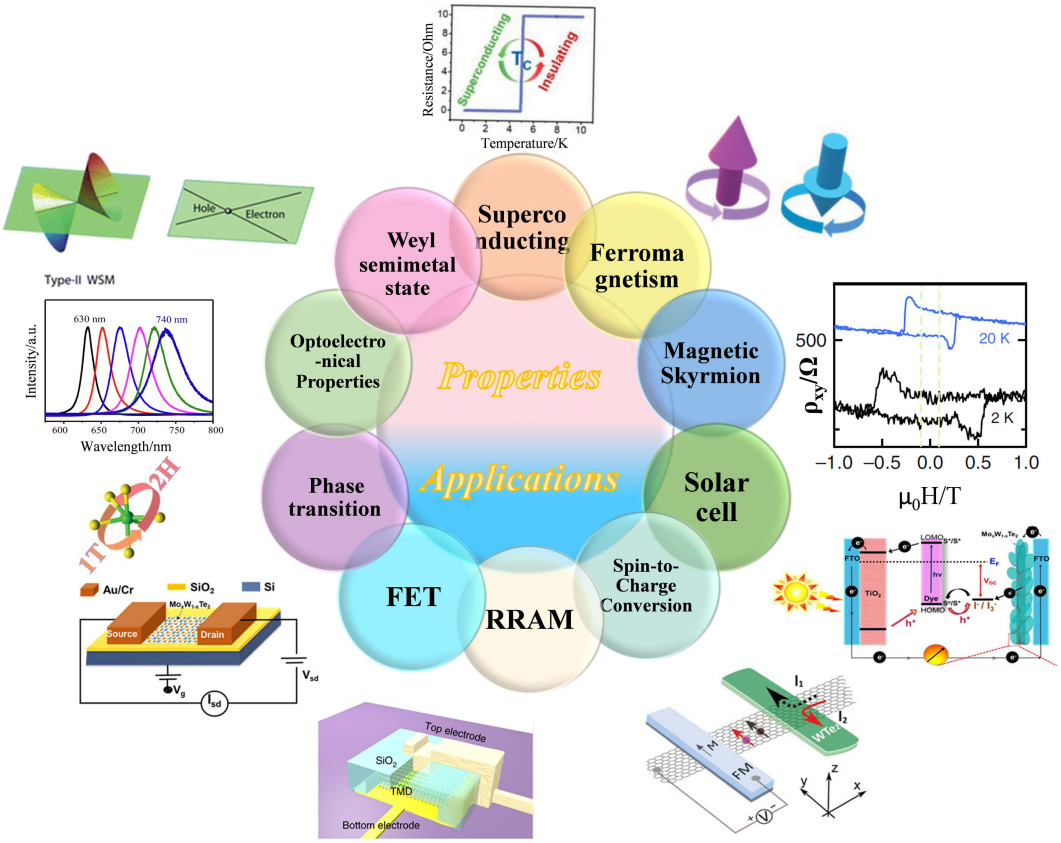


**Figure 1** Physical properties and potential applications of 2D $MoTe_2$, $WTe_2$ and their alloys.

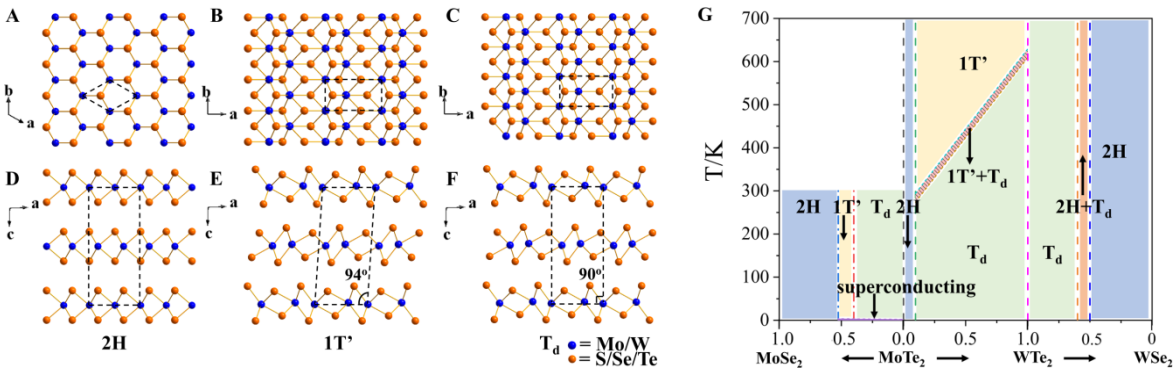


**Figure 2** Crystal structure of $MoTe_2$ and $WTe_2$ in (A, D) 2H phase, (B, E) 1T' phase and (C, F) $T_d$ phase. (G) Phase diagram of $MoSe_2$-$MoTe_2$, $MoTe_2$-$WTe_2$ and $WTe_2$-$WSe_2$.

As increase W doping of $MoTe_2$, the stable phase of $Mo_{1-x}W_xTe$ changes from 2H phase to $T_d$ phase at $x$ = 0.1 when the temperature $T$ < 274 K, while the corresponding stable phase is 1T' phase when $T$ > 294 K. 1T' phase can transfer to $T_d$ phase in the cooling process. And the transition temperature from $T_d$ to 1T' phase increases with the composition of W increasing.[34] This trend is due to the change of phase free energy in $MoTe_2$ with W substitution.[35-36] As increase Se doping of $WTe_2$, the stable phase of $WSe_{2-2x}Te_{2x}$ starts to change from $T_d$ phase to 2H phase at $x$ = 0.6.

In $MoTe_2$, the ligand field stabilization energy ($\Delta_{LFS}$) is close to the CDW phase stabilization energy ($E_{CDW}$), resulting in a small energy difference between the 2H-$MoTe_2$ and $T_d$-$MoTe_2$ phases. For $WTe_2$, the larger W-Te distance reduces $\Delta_{LFS}$ and increases $E_{CDW}$, resulting in a more stable $T_d$ phase.[37] Both $T_d$-$MoTe_2$ and $T_d$-$WTe_2$ have semimetallic band structures (Figures 3A, B).[32-33] The unique electronic structure is from the following two aspects. First, a 0.5 eV overlap of Te 5p- and W 5d-like bands along Γ-Y

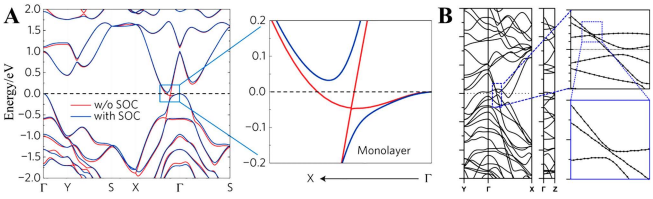


**Figure 3** Band structures of $MoTe_2$ in (A)[32] and $WTe_2$ in (B).[33]

leads to the splitting of $t_{2g}$ orbitals, which contributes to the density of states (DOS) minimum at the Fermi level. Second, electron and hole states form small pockets, which cross the Fermi energy.[38-39] Furthermore, the bulk of $T_d$-$WTe_2$ has a smaller indirect band gap at Γ-point than the monolayer, which contributes to the different electrical behavior of the bulk and monolayer of $T_d$-$WTe_2$.[39]

  

## 3. Preparation

Many methods have been developed to prepare 2D $MoTe_2$, $WTe_2$ and the alloys, such as mechanical exfoliation, MOCVD, MBE, CVD, solution-phase method, and so on. Table 1 summarizes the methods and growth conditions for the preparation of 2D $MoTe_2$, $WTe_2$, and the alloys.

### 3.1. Mechanical exfoliation of bulk crystals

First, bulk single crystals of $MoTe_2$, $WTe_2$ and the alloys are grown by chemical vapor transport (CVT) (Figure 4A) and then the crystals are exfoliated to 2D flakes on substrates. In CVT process, precursors and transport agent are sealed in ampoule, which are then put into a two-zone furnace. Precursors react with the transport agent and yield gaseous compound at one end, and then transport to the other end and decompose to the target materials in the crystal form.[44] The choice of transport agent is important to transport effects because transport rates are proportional to the partial pressure difference of source and sink.[45] And temperature is a vital parameter in CVT process, in order to keep the constant of reaction equilibrium = 1 favoring crystal growth.

2D $MoTe_2$, $WTe_2$, and the alloys are more difficult to be mechanically exfoliated than the sulfides and selenides due to the strong interlayer Te-Te interactions in the tellurides. Au-assistant

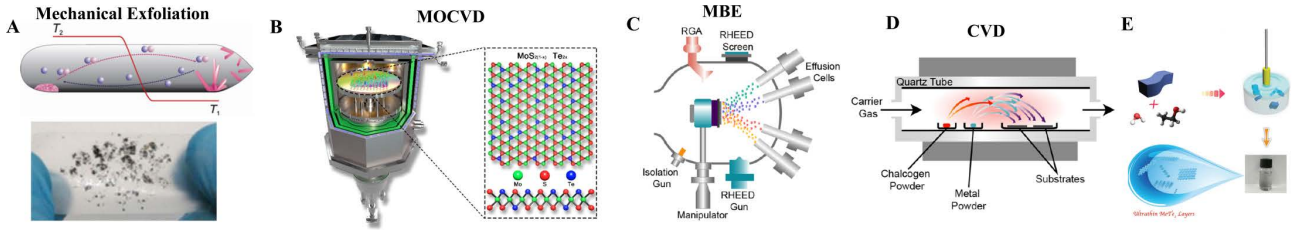


**Figure 4** Illustration of methods for the preparation of $MoTe_2$, $WTe_2$, and the alloys: (A) mechanical exfoliation,[40] (B) MOCVD,[41] (C) MBE,[41] (D) CVD,[42] and (E) solution-phase method.[43]

**Table 1** Summary of the preparation methods for $MoTe_2$, $WTe_2$, and the alloys

| Material | Method | Metal precursors | Assistant | Temperature | Phase | Domain size |
|---|---|---|---|---|---|---|
| $MoTe_2$ | CVT[46] | Mo | $TeBr_4$ | 1000 °C | 1T′ | |
| | CVD[47] | Mo/$MoO_3$ | — | 700 °C | 1T′, 2H | 30 μm |
| | CVD[48] | Mo film | — | 510 °C | 2H | 2.5 cm |
| | CVD[49] | Mo/$MoO_3$ | $FeTe_2$ | 650 °C | 1T′, 2H | 3.2 nm, 4.1 nm |
| | CVD[50] | Mo | — | 650 °C | 1T′, 2H | 10 μm |
| | CVD[51] | $MoO_3$ | NaCl | 650—800 °C | 1T′ | 30 μm |
| | CVD[52] | $MoO_3$ | α-$Al_2O_3$ | 720 °C | 1T′ | 10 μm |
| | CVD[53] | $(NH_4)_6Mo_7O_{24}$ | NaOH, iodixanol | 610 °C | 1T′ | 20 μm |
| | CVD[54] | $(NH_4)_6Mo_7O_{24}$ | $C_{24}H_{41}NaO_6$ | 700 °C | 1T′ | 10 μm |
| | CVD[55] | Mo | | 700 °C | 2H | 2.34 mm |
| | CVD[56] | $MoO_3$ | | 650, 680 °C | 2H,1T′, $T_d$ | 10 μm |
| | CVD[57] | $MoO_2$ | KI | 700 °C | 1T′ | 47 μm |
| | CVD[58] | Mo | | 535—635 °C | 2H, 1T′ | |
| | CVD[59] | $MoO_3$ | | 750 °C | 2H, 1T′ | |
| | CVD[60] | $MoO_3$, $MoCl_5$, Te | | 780 °C | 1T′ | 150 μm |
| | CVD[61] | $(NH_4)_6Mo_7O_{24}\cdot 4H_2O$ | KCl | 750—800 °C | 1T′ | 200 μm |
| | Liquid -phase[43] | $MoTe_2$ | Ethanol | 25 °C | 2H | 500 nm |
| | Liquid -phase[62] | $MoCl_5$, Te | Ethanol | 25 °C | 2H | nanometers |
| | Liquid Phase[63] | $MoTe_2$ | IPA | 25 °C | 2H | 1 μm |
| $WTe_2$ | CVT[64] | W | | 1223 °C | $T_d$ | 48.90 nm |
| | MBE[65] | W | | 250 °C | 1T′ | tens of nm |
| | CVD[61] | $(NH_4)_{10}W_{12}O_{41}\cdot xH_2O$ | KCl | 750—800 °C | 1T′ | 320 μm |
| | CVD[66] | $WCl_6$ | | 500 °C | $T_d$ | tens of nm |
| | CVD[60] | $WO_3$, $WCl_6$, Te | | 820 °C | $T_d$ | 350 μm |
| | CVD[67] | $(NH_4)_2WO_4$ | KI | 700 °C | 1T′ | 7 μm |
| | CVD[68] | W | | 800 °C | $T_d$ | 15 nm |
| | Liquid method[69] | $WCl_6$,Te | oleic acid | 300 °C | $T_d$ | 100 nm |
| | Liquid -phase[62] | $WCl_6$, Te | Ethanol | 25 °C | 2H | nanometers |
| $MoS_{2-x}Te_x$ | CVD[70] | $MoS_2$ | — | 600—700 °C | 2H | 40 μm |
| | CVD[71] | $MoS_2$ | NaOH | 600 °C | 2H | 30 μm |

  

Continued

| Material | Method | Metal precursors | Assistant | Temperature | Phase | Domain size |
|---|---|---|---|---|---|---|
| | CVD[72] | $MoO_3$ | NaCl | 750 °C | 1T′ | |
| | MOCVD[73] | $Mo(CO)_6$ | — | 400 °C | 2H, 1T′ | 10—20 nm |
| $MoSe_{2-x}Te_x$ | CVD[74] | $MoO_3$ | NaCl | 750 °C | 2H | 60 μm |
| | CVD[72] | $MoO_3$ | NaCl | 750 °C | 2 H | |
| | CVD[75] | $MoO_3$ | NaCl | 750 °C | 2H, 1T′, $T_d$ | 50 μm |
| | CVD[76] | $MoO_3$ | NaCl | 700 °C | 2H | 20—30 μm |
| | CVD[76] | $(NH_4)_2MoO_4$ | $C_{24}H_{41}NaO_6$ | 700 °C | 2H | 20 μm |
| | MBE[77] | Mo | | 300 °C | 1T′ | 100 nm |
| $WS_{2-x}Te_x$ | CVD[71] | $WS_2$ | NaOH | 600 °C | 2H | 30 μm |
| | CVD[78] | $WO_3$ | NaCl | 825 °C | 2H, 1T′ | 24 μm |
| | CVD[79] | $WO_3$ | NaCl | 800 °C | 1H, 1T′ | 35—50 μm |
| $WSe_{2-x}Te_x$ | CVT[80] | W | $TeCl_4$ | 980 °C | 2H, $T_d$ | 90 μm |
| | CVT[72,81] | W | $I_2$ | 850-1010 °C | 2H, $T_d$ | 6 mm |
| | CVD[79] | $WO_3$ | NaCl | 800 °C | 1H, 1T′ | 13—23 μm |
| | MBE[82] | W | | 250°C | 2H, 1T′ | |
| $Mo_xW_{1-x}Te_2$ | CVT[83] | Mo, W | $I_2$ | 900-1000 °C | 1T′, $T_d$ | |
| | CVT[84] | Mo, W | $TeCl_4$ | 750 °C | 2H, $T_d$ | |
| | CVT[85] | Mo, W | $Br_2$ | 850 °C | | 9 mm |
| | CVD[86] | $MoO_3$, $WO_3$, $WCl_6$, Te | | 710 °C | 1T′ | Tens of μm |
| | CVD[26] | $WO_3$, $MoO_3$ | NaCl | 700-850 °C | 1T′, $T_d$ | ~100 μm |
| | CVD[87] | $MoO_3$, $WO_3$, $WCl_6$, Te | — | 825 °C | 1T′, $T_d$ | 400 nm |
| | CVD[88] | $MoO_3$, $WO_3$, $WCl_6$, Te | — | 760, 820 °C | 2H, $T_d$ | 300 nm |
| | CVD[89] | $MoO_3$, $WO_3$, $WCl_6$, Te | — | 820 °C | 2H, $T_d$ | Films of ~cm |
| | CVD[31] | Te, $MoO_3$, and $WCl_6$ | — | 680~720 °C | 1T′, $T_d$ | ≈150 nm |
| | Liquid Phase[69] | $MoCl_5$, $WCl_6$, Te | oleic acid | 300 °C | $T_d$ | 100 nm |
| $Cr_xMo_{1-x}Te_2$ | CVT[27] | Mo, Cr | Te | 950 °C | 2H | 0.2mm |
| | Liquid Phase[27] | $Cr_xMo_{1-x}Te_2$ | ethanol | 25 °C | 2H | nanometers |
| $Cr_xW_{1-x}Te_2$ | CVT[28] | W, Cr | Te | 1050 °C | $T_d$ | 3 mm |

mechanical exfoliation technique is helpful to solve this problem.[92-94] As is shown in Figure 5A,[90] an adhesion metal layer (Ti or Cr) is first deposited on $Si/SiO_2$ substrate, then Au film is evaporated on substrate. After that a fresh surface of layered crystal is cleaved from tape and put on the surface of Au film. Millimeter-size monolayer flakes remain on the surface of Au film when the tape is removed. This is because the interaction between Au and $MX_2$ is stronger than interlayer interaction in $MX_2$.[93] Monolayer flakes can be transferred to arbitrary substrates after being etched in $KI/I_2$. Polydimethylsiloxane (PDMS) can be substitute of tape to keep substrate cleaner.[93]

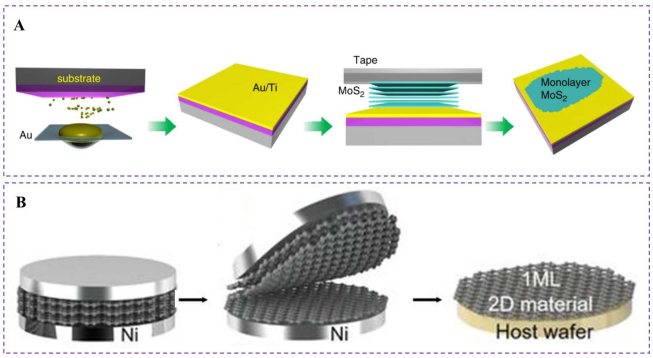


**Figure 5** (A) Schematic illustration of the Au exfoliation process.[90] (B) Mechanical exfoliation process with the assistance of Ni.[91]

A layer-resolved splitting (LRS) method has also been developed to achieve the production of wafer-scale (5 cm) monolayer by splitting single stacks of thick 2D materials grown on a single wafer.[91] As illustrated in Figure 5B, Ni film is deposited on the thick material for splitting 2D material with the substrate. Another Ni film is used for exfoliating the thick material to monolayer.

### 3.2. Metal-organic chemical vapor deposition (MOCVD)

In MOCVD process (Figure 4B), chalcogen and organo-metal precursors are usually used. This method has the advantage of well controllability of precursors partial pressure. But the drawbacks are the slow growth rate and small domain size of the as-prepared thin films.[95]

There are two deposition systems in MOCVD: hot-wall system and cold-wall system. The cold-wall is favorable for minimizing the deposition of precursors on substrate, thus reducing contamination.[41] Few-atomic-layer $MoTe_2$ and $MoS_xTe_{2-x}$ ($0 \le x \le 2$) have been obtained by MOCVD.[73] The percentage of S in the alloy increases with the increase of S/Te molar ratio. But the trend becomes slow down when the S/Te molar ratio is 3.15, which is due to the large difference between the electronegativity and atomic radius of S and Te.[96]

### 3.3. Molecular beam epitaxy (MBE)

MBE can produce 2D crystals with high quality because the utilization of ultra-high vacuum (UHV) system and high purity sources (Figure 4C). This technique is also controllable for the growth of alloys. $WSe_{(2-x)}Te_2$ and $MoSe_{2(1-x)}Te_{2x}$ have been synthe-

  

sized by MBE utilizing highly ordered pyrolytic graphite (HOPG) as substrate. And the growth rate on HOPG is about 3/4 of that when $MoS_2$ is used as a substrate,[77] which is due to the various sticking of Mo-containing precursors on different substrates. Due to the low flux density of Te and the higher enthalpy of formation of W-Te (38 ± 5 kJ/mol) compared to W-Se (185.3 ± 5.5 kJ/mol), more Te precursor concentration is required to realize the incorporation of Te into alloys.[82]

### 3.4. Chemical vapor deposition (CVD)

CVD is a versatile method for the synthesis of 2D $MoTe_2$, $WTe_2$ and the alloys. Mo or $MoO_3$ is usually adopted as the metal precursor for the growth of 2D $MoTe_2$. W or $WCl_6$ is usually used as metal precursor for the growth of 2D $WTe_2$. 2D alloys of $MoTe_2$, $WTe_2$ can be obtained by telluride the binary TMDs or the simultaneous evaporation of chalcogen precursors to react with metal precursors.[26,70-71,74,79] In the reaction process, molecular sieves can be used to control evaporation rate of metal precursors and adsorb the silicon telluride byproducts, thereby controlling the thickness of 2D crystal.[51,97-98] In some works, Te is mixed with metal precursors, for reducing the melting point of metal precursors.

The growth can be one-step growth and two-step growth depending on the experimental details. In the one-step process, metal precursors and substrate are put on the upstream, downstream of the tube, respectively. In a two-step growth, the surface of substrate is covered with metal precursors before CVD growth by magnetron sputtering, evaporation or spin coating. The latter method is easier to obtain monolayer single crystal for the uniform distribution of metal precursor compared to one-step process.

For most works on the CVD growth of 2D $MoTe_2$, $WTe_2$ and the alloys, NaCl/NaOH are usually used as assistant agents. The salts can reduce the melting point of metal oxides and also react with metal oxides to form metal oxychlorides, which can evaporate more easily. Alkali metals (Na, K, Li) decrease the reaction energy barriers and then increase the reaction rate (Figure 6A).[71,101-102] Furthermore, Avetik R. Harutyunyan *et al.* have found that Na ions can act as surfactant (Figure 6B), chemically passivating the surface of monolayer $MoS_2$. This can release in-plane strain, which limits 3D islanding and facilitates 2D growth.[100] Halides also have effects on the reaction dynamics. $MoS_2$ edge is passivated by halogens. And the low Mo-X (X = I, Br, Cl, F, and O) bond dissociation energies ($E_b$) produce low reaction barriers, contributing to a larger crystal size according to Brønsted-Evans-Polanyi (BEP) relation.[103]

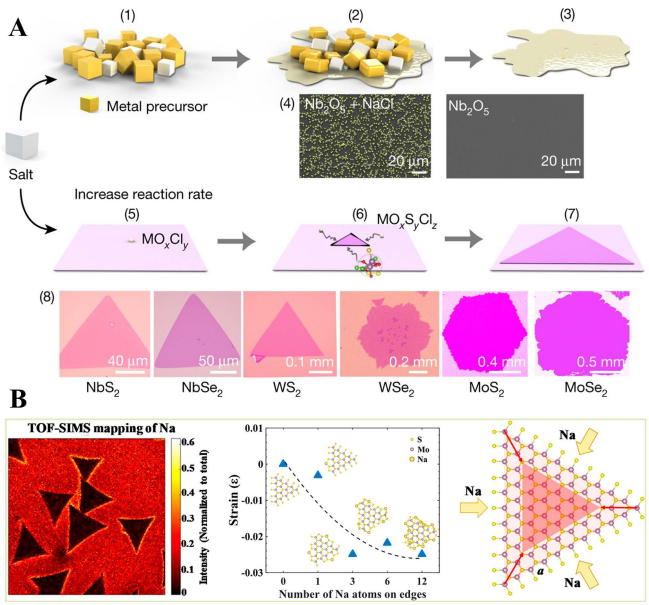


**Figure 6** (A) Reaction mechanism of salt-assisted CVD.[99] (B) The illustration of releasing in-plane strain in 2D materials in the addition of Na in CVD.[100]

The addition of salt facilitates the doping of heteroatoms into binary TMDs. For example, the substitutional doping of Fe, Co, and Mn into $MoS_2$ is realized with the assistance of salt because the volatilization of the dopant precursors is promoted, which alters the electronic structure and phonon properties of $MoS_2$.[104]

Different structural phases of $MoTe_2$ and $WTe_2$ can be obtained by controlling the growth parameters, such as precursors ratio, temperature, gas flow, *etc*. For example, $MoO_3$ or Mo as metal precursor obtains 2H and 1T' $MoTe_2$, respectively. This is because larger strain is induced when Mo transfers to $MoTe_2$, which makes 1T' phase more stable.[47] And 1T' $MoTe_2$ is available with the addition of iodine due to the lower total energy.[57] In addition, 1T' $MoTe_2$ is favored at low temperature and low gas flow. The reason is that the 1T' phase is more stabilized against the 2H phase when Te vacancies is high.[58-59] So insufficient telluride makes the production of 1T' phase easier.[105] For $WTe_2$, 1T' and $T_d$ phases have been prepared, while 2H phase has not been synthetized.

Changing the ratio or heating temperature of precursors is a common way to synthesize 2D alloys of $MoTe_2$, $WTe_2$ with different compositions.[31,74-75,79] Usually, 1T'/$T_d$ phase is favorable when the ratio or heating temperature of Te increases. Gas flow can also change the product composition. For $WS_{2(1-x)}Te_{2x}$, at high Te concentration in mixed alloys, increasing $H_2$ gas flow makes the existence of 1T' phase be favorable.[78] This is because, on the one hand, the reactive activity of Te with $WO_3$ is lower than that of S, but the addition of $H_2$ improves the reactive activity of Te with precursors, increasing the Te component in $WS_{2(1-x)}Te_{2x}$.[79,106-107] On the other hand, the stability of 1T' phase is enhanced at $H_2$ gas flow.[108] Roshan Jesus Mathew *et al*. have found that temperature and cooling rate are the key factors determining the phase of $Mo_xW_{1-x}Te_2$. $T_d$-$Mo_{0.29}W_{0.72}Te_{1.99}$ and 2H-&$T_d$ $Mo_{0.32}W_{0.67}Te_{2.01}$ are grown at 820 °C and 760 °C, respectively. And faster cooling rate contributes to the forming of mono-phase.[89]

### 3.5. Solution-phase method

Solution-phase method includes liquid exfoliation and chemical synthesis in solution phase. The advantages of solution-phase method are low temperature synthesis, easily to obtain dispersions, more choices of substrates and mass production. [63,109]

In the liquid exfoliation method (Figure 7A), bulk materials are mixed with a suitable solvent, followed by ultrasonic exfoliation. The solvent, such as *N*-methyl-pyrrolidone (NMP), ethanol and isopropanol (IPA), is used to minimize the energy of exfoliation.[63] After centrifugation and filtration, 2D $MoTe_2$ nanosheets were obtained.[43] In the chemical synthesis method, 2D telluride can be chemically synthesized in solution phase directly.[27] Figure 7B uncovers that Te nanoparticles can be chemically transformed into $MoTe_2$ or $WTe_2$ thin films. The synthesis enables precise control of

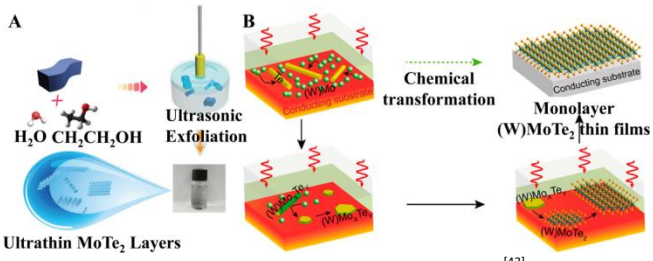


**Figure 7** (A) Liquid exfoliation of $MoTe_2$ nanosheets.[43] (B) Chemical synthesis of $MoTe_2$ and $WTe_2$ in solution phase.[62]

  

the number of atomic layers from a monolayer to multilayers.[62] Yifan Sun *et al*. have synthesized few-layer $WTe_2$ and $Mo_xW_{1-x}Te_2$ nanostructures (30—50 nm). The crystal structure can be adjusted by changing the amount of metal reagent.[69]

## 4. Physical Properties

### 4.1. Structural phase transition

The small energy difference (35 meV/unit cell) between 1T' phase and 2H phase of $MoTe_2$ makes the phase transition easy.[32] For example, selective growth of the 2H phase has been realized by prolonging the reaction time or maintaining excessive Te.[50,55] While annealing of 2H $MoTe_2$ with insufficient Te leads to the growth of the 1T' phase.[55]

Reversible phase transition between 2H and 1T' phase can be used to control the growth from a single nucleus, so as to grow two-dimensional single crystal. For example, Yu Ye *et al*. have fabricated 2.5 cm monolayer 2H $MoTe_2$ from polycrystalline T' $MoTe_2$ film successfully by adopting a single-crystalline 2H $MoTe_2$ nanoflake as crystal seed.[48]

Reversible phase transition of 2D $MoTe_2$, $WTe_2$ and the alloys is appealing for novel devices, such as ohmic-contact homojunctions and phase change memory (PCM) devices.[17,111] Chemical doping as well as external fields, such as pressure,[36] electric field,[17,112] can induce the phase transition. The mechanism of phase transition is relevant to the d-DOS splitting and the competition of the ligand field stabilization energy and the energy of periodic lattice distortion.[37]

The structure phase transition can be characterized by Raman spectroscopy. Figure 8A shows the temperature-dependent Raman spectra of a seven-layer (7L) 1T'-$MoTe_2$ in the cooling process.[110] Both 1T' and $T_d$ $MoTe_2$ contain 12 atoms in a unit cell, leading to 36 vibrational modes. Nevertheless, monoclinic 1T' $MoTe_2$ has 18 Raman-active phonon modes (12 $A_g$ modes and 6 $B_g$ modes, $A_u$ and $B_u$ modes are Raman-inactive), while all the vibrational modes (12 $A_1$ + 6 $A_2$ + 6 $B_1$ + 12 $B_2$) are Raman-active for orthorhombic $T_d$-$MoTe_2$.[113]

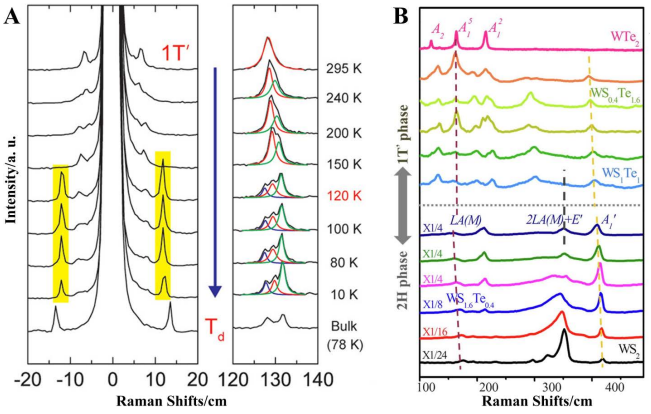


**Figure 8** (A) Raman spectra of 7L 1T'-$MoTe_2$ at various temperature.[110] (B) Raman spectra of $WS_{2(1-x)}Te_{2x}$ with different composition.[78]

As the temperature decreases, phase transition from 1T' phase to $T_d$ phase occurs at 150—120 K, where shear mode $A_1^1$ emerges at ~12 $cm^{-1}$ and $A_g^6$ at ~128 $cm^{-1}$ splits to multiple peaks. But the splitting of $A_g^6$ mode in cooling process occurs before transition temperature at the same time, this phenomenon can also be observed in no-transition sample, suggesting that the emergence of shear mode at ~12 $cm^{-1}$ is the prominent characteristic of 1T'-$T_d$ phase transition.

Additionally, when the thickness of 1T'-$MoTe_2$ is down to ≤ 4 layers (4L), no phase transition occurs in the cooling process. The origin of phase transition may be variations in the local strain. Because the phase transition from 1T' to $T_d$ is realized by relative sliding of adjacent layers, it might be sensitive to local strain.[114]

For 2H-$WS_2$, the in-plane mode (E') at 350 $cm^{-1}$ and the out-of-plane mode ($A_1'$) at 420 $cm^{-1}$ are the characteristic peaks.[115-116] As is shown in Figure 8B,[78] $WS_{2(1-x)}Te_{2x}$ alloy maintains 2H phase as Te composition below 50%, degeneration of 2LA(M) mode and splitting of E' peak around 350 $cm^{-1}$ can be observed due to the introducing of Te atoms. When the Te composition achieves 50%, 2H phase transfers to 1T' phase. The $WS_2$-like E' mode disappears due to the break of W-S mode. At the same time, several Raman peaks appear below 300 $cm^{-1}$, which are related to the W-Te vibration in 1T'-$WTe_2$, like $A_1$ modes at 120 $cm^{-1}$, 132 $cm^{-1}$, 162 $cm^{-1}$ and 213 $cm^{-1}$.[61] When Te composition varies from 0 to 1, the continuous redshift of $A_1'$ maybe arise from the high-frequency vibration caused by the large atomic weight of Te atoms.

STEM is another method to observe phase transition. For $WS_{2(1-x)}Te_{2x}$, the forward and backward offsets of Te atoms from the original 1H lattice sites are discovered by scanning transmission electron microscopy–annular dark field (STEM-ADF).[79] At high Te concentration, higher local displacement of Te atoms breaks hexatomic ring in 1H phase, inducing the transition to 1T' phase.

### 4.2. Optoelectronical properties

The band gap of $MoTe_2$, $WTe_2$ and the alloys varies from 0 to about 2 eV. $MoTe_2$ is applied for ultraviolet, visible light, and infrared detection.[117-120] In addition, Ren *et al*. have found that $T_d$-$WTe_2$ has significant photoresponse in a broadband range from visible to far-infrared at room temperature.[121] And Hongda Li *et al.* have fabricated $MoTe_2$/$WTe_2$ heterostructures, which are candidates for high-speed optoelectronic device with sub-picosecond photo-carrier lifetime.[122]

Composition-dependent alloys exhibit wide range band gap, which is favorable for absorbing or emitting light in a wide spectral range. Figures 9A, B show composition-dependent photoluminescence spectra of $MoS_{2x}Te_{2(1-x)}$ and $WS_{2(1-x)}Te_{2x}$. The PL peaks shift to shorter wavelength as the S composition increases.[78] While no PL peak is found in 1T' phase (Figure 9C).[78]

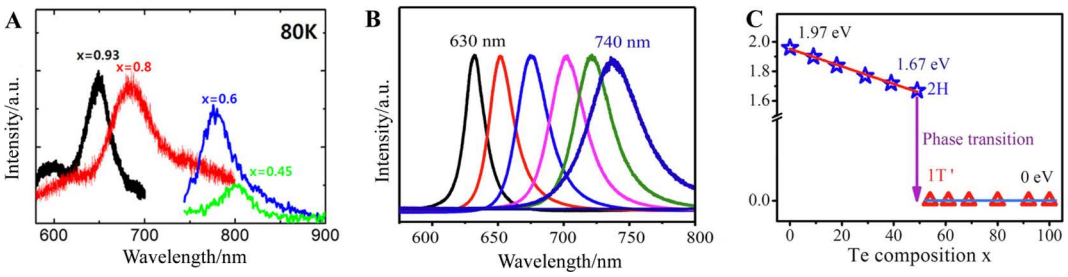


**Figure 9** Composition-dependent photoluminescence spectra of (A) $MoS_{2x}Te_{2(1-x)}$[73] and (B) $WS_{2(1-x)}Te_{2x}$.[78] (C) Composition-dependent band gap in $WS_{2(1-x)}Te_{2x}$.[78]

  

### 4.3. Weyl semimetal state

The magnetoresistance measurements can reveal dynamics of charge carriers and characteristics of Fermi surface of a material. Large magnetoresistance (LMR) is an uncommon property for most of magnetic compounds. As is shown in Figure 10A, an extremely large and non-saturating positive magnetoresistance is obtained in layered $WTe_2$ at low temperatures and high magnetic field.[20] Such exotic behavior is explained in the framework of Fermi surface compensation, which makes $WTe_2$ a possible candidate for type-II Weyl semimetal.

The Weyl semimetal has the non-trivial Fermi-arc surface states that connect the Weyl nodes on the surface Brillouin zone. This chiral anomaly will lead to a negative magnetoresistance owing to the chiral zero modes of the Landau levels of the 3D Weyl cones.[22] As is shown in Figure 10B, gate-tunable negative longitudinal magnetoresistance is observed in layered $WTe_2$.[123] This phenomenon is highly angle-sensitive and is suppressed by a small angle between the electric and magnetic fields, consistent with the distinctive feature of a type-II Weyl semimetal. The direction-dependent negative magnetoresistance is also observed in the layered $Mo_xW_{1-x}Te_2$ (Figure 10C).[26] Further analysis shows a relationship of $Rs(B) \propto -B^2$ at high-field (Figure 10D) that is consistent with the theory expectation of chiral-anomaly-induced negative MR, also proving that $Mo_xW_{1-x}Te_2$ is a type-II Weyl semimetal.[26,123-127] The origin of low-field cusp-like dip (Figure 10B) is weak antilocalization (WAL), which is induced by the spin-orbit coupling (SOC).[18,128-130] And the WAL effect can be enhanced with the decrease of thickness.[130]

### 4.4. Superconductivity

At zero field, the intrinsic superconductivity exists in $MoTe_2$, but it is absent in $WTe_2$. For $MoTe_2$, the superconducting transition temperature $T_c$ is 0.1 K in the bulk, and $T_c$ is 0.5 K in the few-layer. The origin for the enhancement of $T_c$ in thinner layers is the stronger coulomb repulsion interaction in the thinner layers, which is characterized by a predominant W 5d orbital character at the Fermi level.[60]

Superconductivity can emerge in $WTe_2$ at high pressure, via proximity effect, or with chemical doping. In details, superconductivity emerges and LMR effect disappears in $WTe_2$ when pressure increases to 10.5 GPa. A possible explanation is the unbalance between electron and hole populations under elevating pressure.[131] Miao *et al*. have found proximity-induced superconductivity in few-layer $WTe_2$ with $T_c$ = 6.4 K based on $WTe_2/NbSe_2$ van der Waals heterostructure.[132] For chemical doping, Ya Deng *et al*. have observed superconductivity exists in $Mo_xW_{1-x}Te_2$ ($x$ > 0.5) and the superconducting fraction $[R(T_c^{onset}) - R(0.3\ K)]/R(T_c^{onset})$ increases with the rising of Mo fraction (Figure 11A).[26] The linear relation between $H_{c2}$ and T indicates that the measured $Mo_{0.8}W_{0.2}Te_2$ is a 2D superconductor (inset of Figure 11C).[133-135] And R. Dahal *et al*. have found that high pressure increases $T_c$ in $Mo_{1-x}W_xTe_2$, which arises from the softening of the interlayer Te-Te vibration modes.[36,136] Also, superconductivity exists in $K_xWTe_2$ with a $T_c$ of ~2.6 K, which is ascribed to electron-doping effect of K ions. And the original structure of $WTe_2$ has not been damaged, which exhibits that $WTe_2$ is still of the topological nontrivial state.[137]

Dramatic enhancement of superconductivity enhancement has been observed in Se- and S-doped $T_d$-$MoTe_2$ bulk samples (Figure 11B).[75,138] Compared with the pristine $MoTe_2$, $T_c$ is improved by nearly 13-fold in the $MoTe_{1.8}S_{0.2}$ and 36-fold in the MoSeTe. The magnetotransport measurements demonstrate the potential $s_{+-}$-wave two-band superconductivity due to a dominant interband coupling.[75] The enhanced $T_c$ can be explained by the introduction of low-diffusivity electrons by the S or Se substitutions, which may have a larger superconducting gap. As seen from Figure 11D, the simulation fitted by the two-band model is consistent with the experimental data.[75]

### 4.5. Ferromagnetism

The intrinsic ferromagnetism in 2D materials offers the opportunity to spintronic devices.[139-141] It is also vital to realize the magnetic control of topological phase and quantum anomalous Hall effect.[142-146] But it is still challenging and more exploration is needed.

The pure $WTe_2$ bulk material is diamagnetic. By introducing

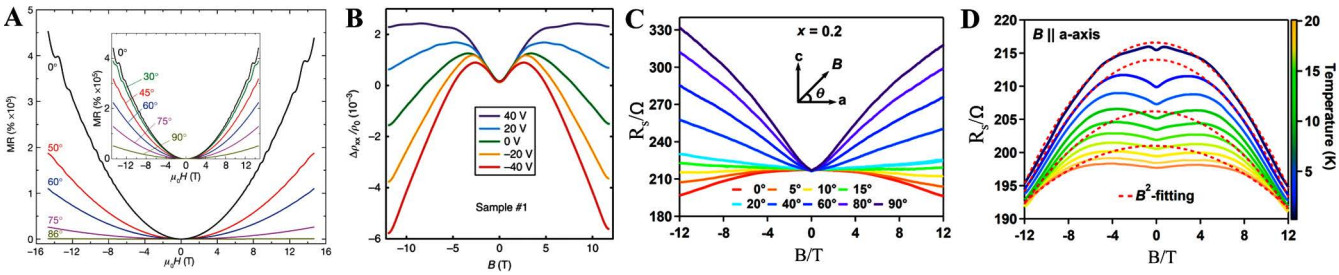


**Figure 10** (A, C) The magnetoresistance versus magnetic field of $WTe_2$, $Mo_xW_{1-x}Te_2$ in different angle between the magnetic field and the crystal *c*, *a* axis, respectively.[20,26] (B) The magnetoresistance versus magnetic field of $WTe_2$ at various gate voltages.[123] (D) The magnetoresistance of $Mo_xW_{1-x}Te_2$ at various temperatures.[26]

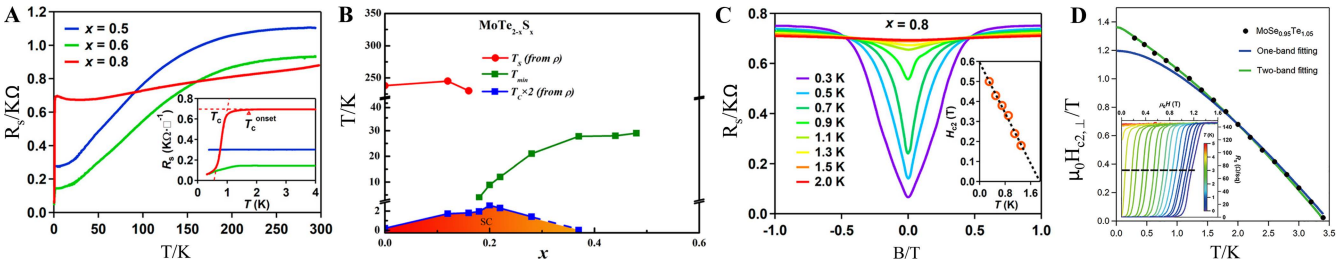


**Figure 11** (A) The *R*-*T* behavior of $Mo_xW_{1-x}Te_2$.[26] (B) The phase diagram of $MoTe_{2-x}S_x$.[138] (C) Magnetic field dependence of $R_s$ in pristine $Mo_{0.8}W_{0.2}Te_2$ sample at various temperatures.[26] (D) Temperature dependence of perpendicular upper critical field $\mu_0H_{c2,\perp}$ for $MoSe_{0.95}Te_{1.05}$ thin films.[75]

  

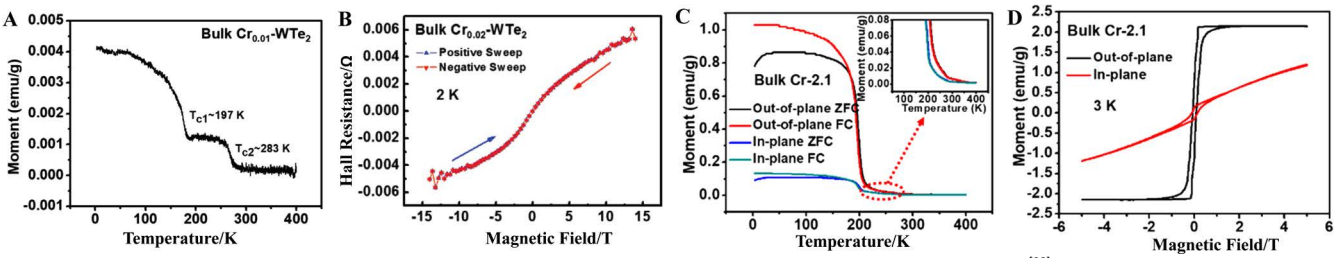


**Figure 12** (A) Temperature dependence of magnetic moment in bulk $Cr_{0.01}$-$WTe_2$ under zero external magnetic field.[28] (B) Anomalous Hall effect (AHE) for $Cr_{0.02}$–$WTe_2$ samples with magnetic field range from −14 to 14 T.[28] (C) *M-T* curves and (D) *M-H* curves of bulk Cr-2.1 $MoTe_2$ sample with magnetic field applied along the out-of-plane and in-plane direction.[27]

the Cr element into layered $T_d$-$WTe_2$, near-room temperature ferromagnetism with a Curie temperature ($T_c$) of up to 283 K is successfully achieved.[28] The $T_c$ and saturated magnetic moment can be well tuned by the Cr valence states, which are closely related to the doping concentrations of Cr.[147-148] Bulk $Cr_{0.01}$-$WTe_2$ has two $T_c$ (Figure 12A), which is attributed to the coexistence of high and low valence states of Cr. The saturation magnetic moment is changed from 2.26 emu·g$^{-1}$ for $Cr_{0.01}$-$WTe_2$ to 4.20 emu·g$^{-1}$ for $Cr_{0.02}$-$WTe_2$. The long-range order of ferromagnetism is also confirmed by the electrical transport properties. The Hall resistance of Cr-doped $WTe_2$ shows a clear "S" shape (Figure 12B), which is attributed to the anomalous Hall effect (AHE).

More robust ferromagnetism is also found in the layered Cr-doped 2H-$MoTe_2$.[27] By regulating the Cr doping concentration, the highest $T_c$ of up to 275 K and the highest $M_s$ of 4.78 emu·g$^{-1}$ have been achieved. Most intriguingly, the magnetization curves of all Cr-doped $MoTe_2$ crystals display obvious hysteresis loops with a strong magnetic anisotropy along the out-of-plane direction (Figures 12 C&D), which indicates the intrinsic ferromagnetism rather than the defect-induced ferromagnetism in Cr-doped $MoTe_2$.

## 5. Device Applications

### 5.1. Field-effect transistors (FETs)

FET is a basic component of the integrated circuit. 2D $MoTe_2$, $WTe_2$ and the alloys have attracted much attention for the high mobility, ferromagnetic properties, ambipolar properties.[149-150] For $T_d$-$WTe_2$, it has high mobility up to 2100 cm$^2$·V$^{-1}$·s$^{-1}$.[132] But semimetal properties inhibit its application in FETs. Fortunately, doping can open up a band gap.[78] For example, for $Mo_xW_{1-x}Te_2$, with the increase of Mo doping, phase transition from $T_d$ to 2H occurs.[88] The transfer curves of FET indicate the corresponding semimetal, p-type semiconductor behaviors. Figure 13A illustrates the structure of FET. Furthermore, as shown in Figure 13B, with the rise of Se doping percent, ambipolar behavior in $MoSe_{2x}Te_{2-2x}$ transfers to n-type behavior arising from the increase of band gap.[151] This phenomenon can be explained by the theory of Schottky-barrier field effect transistors (SBFETs).[152-156] For $MoS_{2x}Te_{2-2x}$, as the increase of S content, the conduction behavior changes from p-type to n-type and the on/off ratio rises due to the larger band gap (Figure 13C).[73]

### 5.2. Resistive random access memory (RRAM)

Memory devices are essential building blocks in integrated electronic system.[157] Appenzeller and co-workers have fabricated the $Mo_{1-x}W_xTe_2$ and 2H $MoTe_2$-based memory devices (Figure 14A).[17] As the bias voltage increases, phase transition happens (2H to 1T') accompanying conductivity change from high resistive state (HRS) to low resistive state (LRS) (Figure 14B). Set voltage lowers for thinner $Mo_{1-x}W_xTe_2$. And $Mo_{1-x}W_xTe_2$ needs lower set voltage than $MoTe_2$ (Figure 14C). Therefore, $Mo_{1-x}W_xTe_2$-based RRAM exhibits higher performance. This interesting result provides the possibility of potential application for $MoTe_2$ and $WTe_2$ based nonvolatile memory.

### 5.3. Spin-to-charge conversion

The efficient generation and control of spin polarization via charge-to-spin conversion (CSC) in topological materials are desirable for future spintronic and quantum technologies.[158-161] An outstanding feature of 2D $MoTe_2$, $WTe_2$ and the alloys is their novel spin topology in the electronic band structures with unexpected large CSC efficiency. By using the spin-torque ferromagnetic resonance (ST-FMR) technique, the CSC efficiency in $WTe_2$/Py samples is evaluated (Figure 15A).[158] The thickness-dependent CSC efficiency of the bulk $WTe_2$ layer reaches 0.51 at 6—7 GHz and the interfacial DMI is as large as −1.78 mJ·m$^{-2}$ (Figure 15B).[158] A charge current density of ~2.96 × 10$^5$ A·cm$^{-2}$ suffices to switch the magnetization of the Py layer (Figure 15C). Controlling spin–orbit torques by crystal symmetries is also achieved in $WTe_2$/Py bilayers (Figure 15D).[159] An out-of-plane antidamping torque is generated when current is applied along a low-symmetry axis of bilayer sample, but vanished when current is applied along a high-symmetry axis.[159]

The highly efficient and unconventional CSC is also observed in the $WTe_2$/graphene heterostructure spin-valve device at room temperature.[160-161] The detected spin polarization in $WTe_2$ is different from the conventional bulk spin Hall effect and surface states dominated Rashba–Edelstein effect. The unconventional

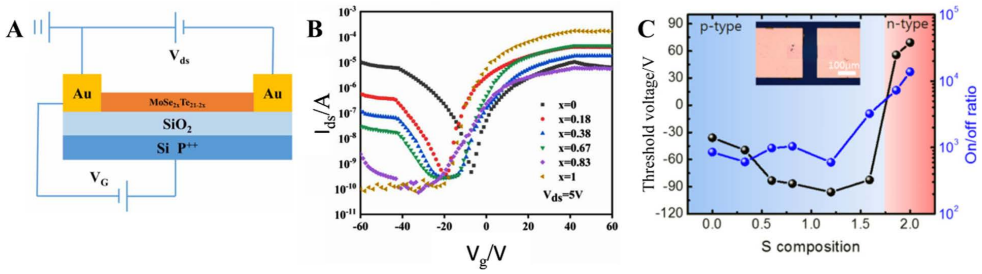


**Figure 13** (A) Schematic diagam of FET structure.[151] (B) Transfer characteristic ($I_{ds}$–$V_g$) of $MoSe_{2x}Te_{2-2x}$ ($x$ = 0—1) alloys.[151] (C) Composition-dependent threshold voltages and on/off ratios of $MoS_{2x}Te_{2(1-x)}$ ($0 \le x \le 1$) atomic layers.[73]

  

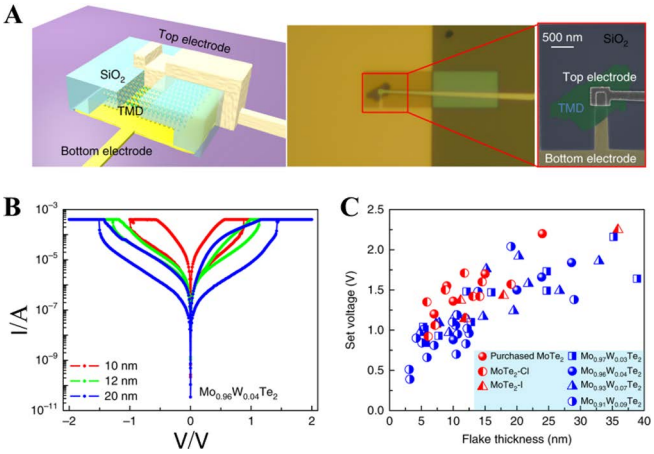


**Figure 14** (A) Schematic of RRAM device structure. (B) *I-V* curves of $Mo_{0.96}W_{0.04}Te_2$. (C) Set voltages of $MoTe_2$ with different fabrication method and $Mo_{1-x}W_xTe_2$ with $x$ = 0—1.[17]

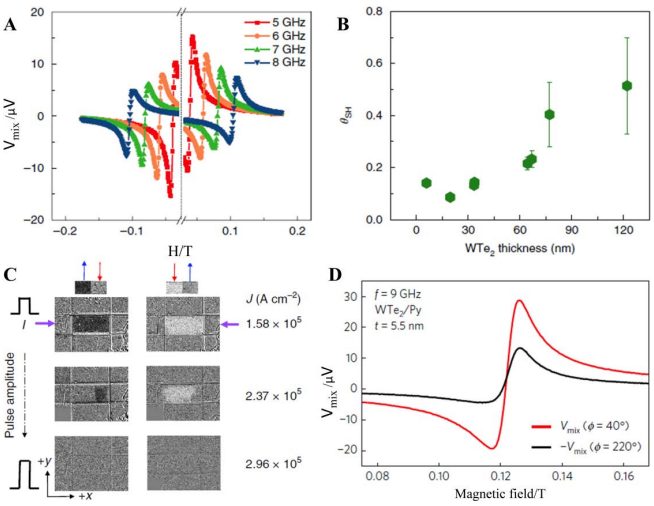


**Figure 15** (A) The ST-FMR spectra for the $WTe_2$(19.6 nm)/Py(6 nm) device with the current in the *b*-axis and $\vartheta$ = 40°.[158] (B) The thickness-dependent CSC efficiency of $WTe_2$ from ST-FMR averaged between 6 and 7 GHz.[158] (C) The switching process of $WTe_2$/Py bilayer captured by MOKE images.[158] (D) ST-FMR resonances for a $WTe_2$(5.5 nm)/Py(6 nm) sample with current applied along the *a*-axis, with the magnetization oriented at 40° and 220° relative to the current direction.[159]

spin conductivity in $WTe_2$ is allowed by considering strain as well as the $WTe_2$/graphene interface to break the crystal symmetry (Figure 16).[160] This indicates that $WTe_2$ can be utilized for spin injection and detection in the all van der Waals heterostructure devices.

### 5.4. Solar cell

Topological Weyl semi-metals (TWS) hold great potentials in electrocatalytic applications.[162-166] In TWS, the conduction bands and valence bands cross near the Fermi energy level, *i.e.*, Weyl points, which can increase charge mobility as well as fasten electron–hole separation and then decrease the electron–hole recombination.[167-169] In addition, topologically protected surface states of TWS are free from impurity/defect scattering which favors charge transport.[170-173] As is shown in Figure 17, Shemsia Mohammed Hudie and co-workers have utilized $Mo_xW_{1-x}Te_2$ as the counter electrode (CE) of dye-sensitized solar cells (DSSCs).[88] The result shows that the efficiency and photocurrent densities of $T_d$-$Mo_xW_{1-x}Te_2$ are both higher than those of Pt electrode and $T_d$-&2H-$Mo_xW_{1-x}Te_2$ (Figures 17B, C).

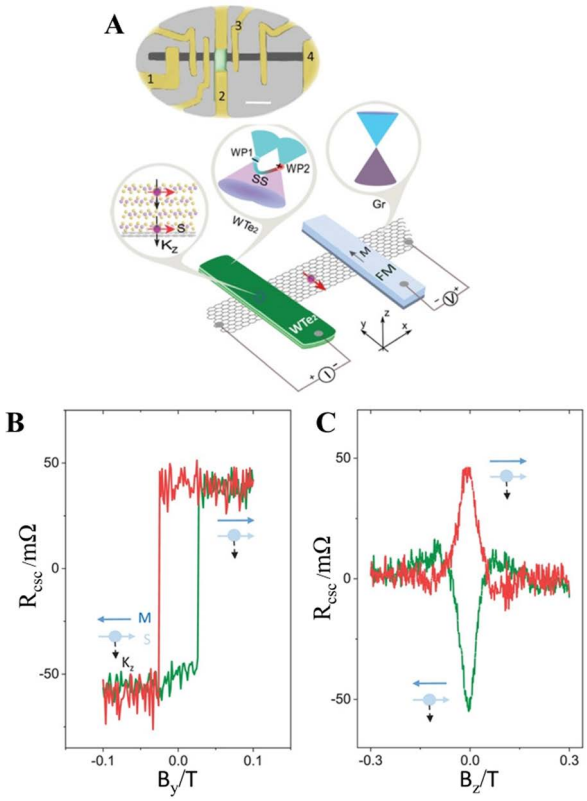


**Figure 16** (A) Schematic of measurement geometry and colored device picture for electrical detection of unconventional CSC in $WTe_2$. (B—C) The nonlocal spin-valve measurement and corresponding Hanle spin precession signal observed in $WTe_2$/graphene heterostructure at room temperature.[160]

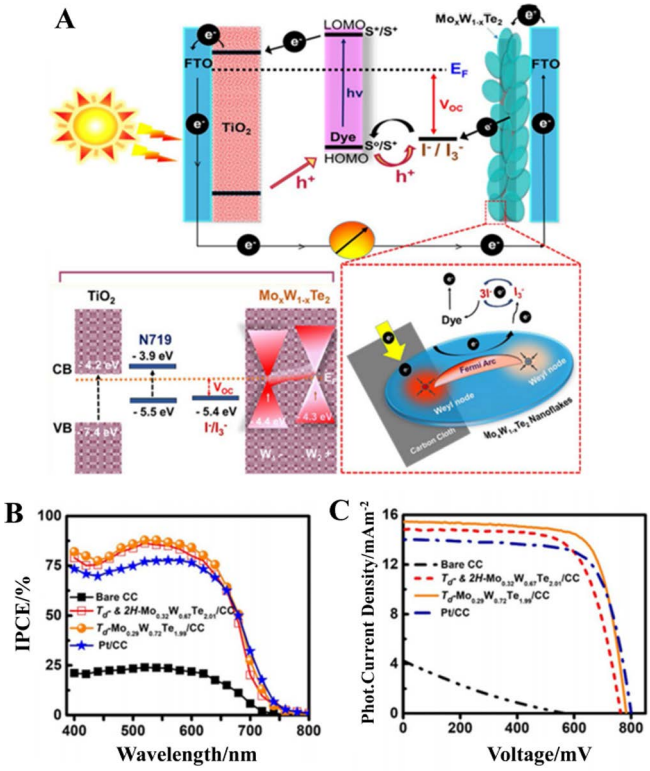


**Figure 17** (A) Illustration of working mechanism in dye-sensitized solar cells. The IPCE (B) and *J-V* (C) curves of $T_d$-$Mo_{0.29}W_{0.72}Te_{1.99}$/CC, Pt/CC electrodes, bare CC, and Td- & 2H-$Mo_{0.32}W_{0.67}Te_{2.01}$/CC.[88]

  

## 6. Conclusions and Perspectives

In conclusion, we have discussed the preparation, properties, and applications of 2D $MoTe_2$, $WTe_2$ and their alloys. However, so far, research on the atomic-thickness $MoTe_2$, $WTe_2$ and their alloys is still in its infancy. For fabrication, considering the strong interlayer interaction, mechanical exfoliation is of low efficiency, which restricts its practical applications. CVD method holds the potential for mass production with high quality and low cost. But the poor reactivity of Te makes the CVD synthesis difficult. MBE and MOCVD can yield clean and high-quality samples but with high cost, small domain size. Solution-phase method exhibits the traits of low temperature, easily to obtain dispersions, more choices of substrates and mass production. In the synthesis and post process of the 2D tellurides, the poor air stability and high chemical activity is a trouble issue. In the property and device aspects, Weyl semimetal state, optoelectronical properties, superconductivity, and ferromagnetism are fascinating properties in 2D $MoTe_2$, $WTe_2$ and their alloys. Based on these promising properties, 2D $MoTe_2$, $WTe_2$ and their alloys hold potentials for FETs, memory devices, spintronic devices, energy, and so on. 2D $MoTe_2$, $WTe_2$ and their alloys are also promising for static random-access memory, logical NOT-AND gate, and five-stage ring oscillator.

## Acknowledgement

L.X. acknowledges support from NSFC (21822502), the Key Research Program of Frontier Sciences of CAS (QYZDB-SSW-SYS031) and the Strategic Priority Research Program of CAS (XDB30000000). Y. C. acknowledges support from the National Basic Research of China (2017YFA0206300) and NSFC (51972335).

## References

[1] Novoselov, K. S.; Geim, A. K.; Morozov, S. V.; Jiang, D.; Zhang, Y.; Dubonos, S. V.; Grigorieva, I. V.; Firsov, A. A. Electric field effect in atomically thin carbon films. *Science* **2004**, *306*, 666–674.

[2] Watanabe, K.; Taniguchi, T.; Kanda, H. Direct-bandgap properties and evidence for ultraviolet lasing of hexagonal boron nitride single crystal. *Nat. Mater.* **2004**, *3*, 404–409.

[3] Mattheis, L. F. Band structures of transition-metal-dichalcogenide layer compouds. *Phys. Rev. B* **1973**, *8*, 3719–3740.

[4] Bhimanapati, G. R.; Lin, Z.; Meunier, V.; Jung, Y.; Cha, J.; Das, S.; Xiao, D.; Son, Y.; Strano, M. S.; Cooper, V. R.; Liang, L. B.; Louie, S. G.; Ringe, E.; Zhou, W.; Kim, S. S.; Naik, R. R.; Sumpter, B. G.; Terrones, H.; Xia, F. N.; Wang, Y. L.; Zhu, J.; Akinwande, D.; Alem, N.; Schuller, J. A.; Schaak, R. E.; Terrones, M.; Robinson, J. A. Recent Advances in Two-Dimensional Materials beyond Graphene. *ACS Nano* **2015**, *9*, 11509–11539.

[5] Tran, V.; Soklaski, R.; Liang, Y. F.; Yang, L. Layer-controlled band gap and anisotropic excitons in few-layer black phosphorus. *Phys. Rev. B* **2014**, *89*, 6.

[6] Bie, Y.-Q.; Grosso, G.; Heuck, M.; Furch, M. M.; Cao, Y.; Zheng, J.; Bunandar, D.; Navarro-Moratalla, E.; Zhou, L.; Efetov, D. K.; Taniguchi, T.; Watanabe, K.; Kong, J.; Jarillo-Herrero, D. E. P. A $MoTe_2$-based light-emitting diode and photodetector for silicon photonic integrated circuits. *Nat. Nanotechnol.* **2017**, *12*, 1124.

[7] Jariwala, D.; Sangwan, V. K.; Lauhon, L. J.; Marks, T. J.; Hersam, M. C. Emerging Device Applications for Semiconducting Two-Dimensional Transition Metal Dichalcogenides. *ACS Nano* **2014**, *8*, 1102–1120.

[8] Akinwande, D.; Petrone, N.; Hone, J. Two-dimensional flexible nanoelectronics. *Nat. Commun.* **2014**, *5*, 5678.

[9] Hussain, S.; Patil, S. A.; Vikraman, D.; Mengal, N.; Liu, H.; Song, W.; An, K.-S.; Jeong, S. H.; Kim, H.-S.; Jung, J. Large area growth of $MoTe_2$ films as high performance counter electrodes for dye-sensitized solar cells. *Sci. Rep.* **2018**, *8*, 29.

[10] Feng, Q.; Zhu, Y.; Hong, J.; Zhang, M.; Duan, W.; Mao, N.; Wu, J.; Xu, H.; Dong, F.; Lin, F.; Jin, C.; Wang, C.; Zhang, J.; Xie, L. Growth of large-area 2D $MoS_{2(1-x)}$ $Se_{2x}$ semiconductor alloys. *Adv. Mater.* **2014**, *26*, 2648–2653.

[11] Feng, Q.; Mao, N.; Wu, J.; Xu, H.; Wang, C.; Zhang, J.; Xie, L. Growth of $MoS_{2(1-x)}Se_{2x}$ (x = 0.41–1.00) Monolayer Alloys with Controlled Morphology by Physical Vapor Deposition. *ACS Nano* **2015**, *9*, 7450–7455.

[12] Chen, Y.; Xi, J.; Dumcenco, D. O.; Liu, Z.; Kazu, S.; Wang, D.; Shuai, Z.; Huang, Y.; Xie, L. Tunable Band Gap Photoluminescence from Atomically Thin Transition-Metal Dichalcogenide Alloys. *ACS Nano* **2013**, *7*, 4610–4616.

[13] Miyauchi, Y.; Konabe, S.; Wang, F.; Zhang, W.; Hwang, A.; Hasegawa, Y.; Zhou, L.; Mouri, S.; Toh, M.; Eda, G.; Matsuda, K. Evidence for line width and carrier screening effects on excitonic valley relaxation in 2D semiconductors. *Nat. Commun.* **2018**, *9*, 2598.

[14] Mak, K. F.; He, K.; Shan, J.; Heinz, T. F. Control of valley polarization in monolayer $MoS_2$ by optical helicity. *Nat. Nanotechnol.* **2012**, *7*, 494–498.

[15] Echeverry, J. P.; Urbaszek, B.; Amand, T.; Marie, X.; Gerber, I. C. Splitting between bright and dark excitons in transition metal dichalcogenide monolayers. *Phys. Rev. B* **2016**, *93*, 121107.

[16] Li, Y.; Duerloo, K.; Wauson, K.; Reed, E. J. Structural semiconductor-to-semimetal phase transition in two-dimensional materials induced by electrostatic gating. *Nat. Commun.* **2016**, *7*, 10671.

[17] Zhang, F.; Zhang, H.; Krylyuk, S.; Milligan, C. A.; Zhu, Y.; Zemlyanov, D. Y.; Bendersky, L. A.; Burton, B. P.; Davydov, A. V.; Appenzeller, J. Electric-field induced structural transition in vertical $MoTe_2$- and $Mo_{(1-x)}W_xTe_2$-based resistive memories. *Nat. Mater.* **2019**, *18*, 55–61.

[18] Jiang, J.; Tang, F.; Pan, X. C.; Liu, H. M.; Niu, X. H.; Wang, Y. X.; Xu, D. F.; Yang, H. F.; Xie, B. P.; Song, F. Q.; Dudin, P.; Kim, T. K.; Hoesch, M.; Das, P. K.; Vobornik, I.; Wan, X. G.; Feng, D. L. Signature of Strong Spin-Orbital Coupling in the Large Nonsaturating Magnetoresistance Material $WTe_2$. *Phys. Rev. Lett.* **2015**, *115*, 166601.

[19] Zhang, E.; Chen, R.; Huang, C.; Yu, J.; Zhang, K.; Wang, W.; Liu, S.; Ling, J.; Wan, X.; Lu, H. Z.; Xiu, F. Tunable Positive to Negative Magnetoresistance in Atomically Thin $WTe_2$. *Nano Lett.* **2017**, *17*, 878–885.

[20] Ali, M. N.; Xiong, J.; Flynn, S.; Tao, J.; Gibson, Q. D.; Schoop, L. M.; Liang, T.; Haldolaarachchige, N.; Hirschberger, M.; Ong, N. P.; Cava, R. J. Large, non-saturating magnetoresistance in $WTe_2$. *Nature* **2014**, *514*, 205–208.

[21] Sanfeng; Fatemi; Valla; Gibson; Quinn, D.; Watanabe; Kenji; Taniguchi; Takashi; Va, C. Observation of the quantum spin Hall effect up to 100 kelvin in a monolayer crystal. *Science* **2018**, *359*, 76–79.

[22] Yan, B.; Felser, C. Topological Materials: Weyl Semimetals. *Annu. Rev. Condens. Matter Phys.* **2017**, *8*, 337–354.

[23] Soluyanov, A. A.; Gresch, D.; Wang, Z.; Wu, Q.; Troyer, M.; Dai, X.; Bernevig, B. A. Type-II Weyl semimetals. *Nature* **2015**, *527*, 495–498.

[24] Qian, X.; Liu, J.; Fu, L.; Li, J. Quantum spin Hall effect in two-dimensional transition metal dichalcogenides. *Science* **2014**, *346*, 1344–1347.

[25] Muechler, L.; Alexandradinata, A.; Neupert, T.; Car, R. Topological Nonsymmorphic Metals from Band Inversion. *Phys. Rev. X* **2016**, *6*, 041069.

[26] Deng, Y.; Li, P.; Zhu, C.; Zhou, J.; Wang, X.; Cui, J.; Yang, X.; Tao, L.; Zeng, Q.; Duan, R.; Fu, Q.; Zhu, C.; Xu, J.; Qu, F.; Yang, C.; Jing, X.; Lu, L.; Liu, G.; Liu, Z. Controlled Synthesis of $Mo_xW_{1-x}Te_2$ Atomic Layers with Emergent Quantum States. *ACS Nano* **2021**, *15*, 11526–11534.

[27] Yang, L.; Wu, H.; Zhang, L.; Zhang, G.; Li, H.; Jin, W.; Zhang, W.; Chang, H. Tunable and Robust Near-Room-Temperature Intrinsic Ferromagnetism of a van der Waals Layered Cr-Doped 2H-$MoTe_2$ Semiconductor with an Out-of-Plane Anisotropy. *ACS Appl. Mater. Inter.* **2021**, *13*, 31880–31890.

[28] Yang, L.; Wu, H.; Zhang, L.; Zhang, W.; Li, L.; Kawakami, T.; Sugawara, K.; Sato, T.; Zhang, G.; Gao, P.; Muhammad, Y.; Wen, X.; Tao, B.; Guo, F.; Chang, H. Highly Tunable Near-Room Temperature Ferromagnetism in Cr-Doped Layered $T_d$-$WTe_2$. *Adv. Funct. Mater.* **2021**, *31*,

  

08116.
[29] Keum; Dong, H.; Hee, Y.; Gang, H.; Joon, S.; Duong, D. L. van der Waals Metallic Transition Metal Dichalcogenides. *Chem. Rev.* **2018**, *118*, 6297–6336.
[30] Sokolikova, M. S.; Mattevi, C. Direct synthesis of metastable phases of 2D transition metal dichalcogenides. *Chem. Soc. Rev.* **2020**, *49*, 3952–3980.
[31] Zou, Y. C.; Chen, Z. G.; Liu, S.; Aso, K.; Zhang, C.; Kong, F.; Hong, M.; Matsumura, S.; Cho, K.; Zou, J. Atomic Insights into Phase Evolution in Ternary Transition-Metal Dichalcogenides Nanostructures. *Small* **2018**, *14*, 1800780.
[32] Dong, H. K.; Cho, S.; Kim, J. H.; Choe, D. H.; Lee, Y. H. Bandgap opening in few-layered monoclinic $MoTe_2$. *Nat. Phys.* **2015**, *11*, 482–U144.
[33] Lee, C. H.; Silva, E. C.; Calderin, L.; Nguyen, M. A.; Hollander, M. J.; Bersch, B.; Mallouk, T. E.; Robinson, J. A. Tungsten ditelluride: a layered semimetal. *Sci. Rep.* **2015**, *5*, 10013.
[34] Lv, Y. Y.; Cao, L.; Li, X.; Zhang, B. B.; Wang, K.; Bin, P.; Ma, L.; Lin, D.; Yao, S. H.; Zhou, J.; Chen, Y. B.; Dong, S. T.; Liu, W.; Lu, M. H.; Chen, Y.; Chen, Y. F. Composition and temperature-dependent phase transition in miscible $Mo_{1-x}W_xTe_2$ single crystals. *Sci. Rep.* **2017**, *7*, 44587.
[35] Yan, X.-J.; Lv, Y.-Y.; Li, L.; Li, X.; Yao, S.-H.; Chen, Y.-B.; Liu, X.-P.; Lu, H.; Lu, M.-H.; Chen, Y.-F. Composition dependent phase transition and its induced hysteretic effect in the thermal conductivity of $W_xMo_{1-x}Te_2$. *Appl. Phys. Lett.* **2017**, *110*, 211904.
[36] Dahal, R.; Deng, L. Z.; Poudel, N.; Gooch, M.; Wu, Z.; Wu, H. C.; Yang, H. D.; Chang, C. K.; Chu, C. W. Tunable structural phase transition and superconductivity in the Weyl semimetal $Mo_{1-x}W_xTe_2$. *Phys. Rev. B* **2020**, *101*, 140505.
[37] K C, S.; Zhang, C.; Hong, S.; Wallace, R. M.; Cho, K. Phase stability of transition metal dichalcogenide by competing ligand field stabilization and charge density wave. *2D Mater.* **2015**, *2*, 035019.
[38] Augustin, J.; Eyert, V.; Boker, T.; Frentrup, W.; Dwelk, H.; Janowitz, C.; Manzke, R. Electronic band structure of the layered compound Td-$WTe_2$. *Phys. Rev. B* **2000**, *62*, 10812–10823.
[39] Jana, M. K.; Singh, A.; Late, D. J.; Rajamathi, C. R.; Biswas, K.; Felser, C.; Waghmare, U. V.; Rao, C. N. R. A combined experimental and theoretical study of the structural, electronic and vibrational properties of bulk and few-layer $T_d$-$WTe_2$. *J. Phys. Condens. Matter* **2015**, *27*, 285401.
[40] Wang, X.; Xie, L.; Zhang, J. Preparation, Structure and Properties of Two-dimensional Semiconductor Alloys. *Acta Chim. Sinica* **2015**, *73*, 886–894.
[41] Briggs, N.; Subramanian, S.; Lin, Z.; Li, X.; Zhang, X.; Zhang, K.; Xiao, K.; Geohegan, D.; Wallace, R. M.; Chen, L. A roadmap for electronic grade 2D materials. *2D Mater.* **2019**, *6*, 022001.
[42] Lin, Y. C.; Torsi, R.; Geohegan, D. B.; Robinson, J. A.; Xiao, K. Controllable Thin-Film Approaches for Doping and Alloying Transition Metal Dichalcogenides Monolayers. *Adv. Sci.* **2021**, *8*, 2004249.
[43] Liu, X.; Yang, H.; He, J.; Liu, H.; Song, L.; Li, L.; Luo, J. Highly Active, Durable Ultrathin $MoTe_2$ Layers for the Electroreduction of $CO_2$ to $CH_4$. *Small* **2018**, *14*, 1704049.
[44] Gruehn, R.; Glaum, R. New results of chemical transport as a method for the preparation and thermochemical investigation of solids. *Angew. Chem. Int. Ed.* **2000**, *39*, 692–716.
[45] Binnewies, M.; Schmidt, M.; Schmidt, P. Chemical Vapor Transport Reactions-Arguments for Choosing a Suitable Transport Agent. *Z. Anorg. Allg. Chem.* **2017**, *643*, 1295–1311.
[46] Chen, S. Y.; Naylor, C. H.; Goldstein, T.; Johnson, A. T.; Yan, J. Intrinsic Phonon Bands in High-Quality Monolayer T' Molybdenum Ditelluride. *ACS Nano* **2017**, *11*, 814–820.
[47] Zhou, L.; Xu, K.; Zubair, A.; Liao, A. D.; Fang, W.; Ouyang, F.; Lee, Y. H.; Ueno, K.; Saito, R.; Palacios, T.; Kong, J.; Dresselhaus, M. S. Large-Area Synthesis of High-Quality Uniform Few-Layer $MoTe_2$. *J. Am. Chem. Soc.* **2015**, *137*, 11892–11895.
[48] Xu, X.; Pan, Y.; Liu, S.; Han, B.; Gu, P.; Li, S.; Xu, W.; Peng, Y.; Han, Z.; Chen, J.; Gao, P.; Ye, Y. Seeded 2D epitaxy of large-area single-crystal films of the van der Waals semiconductor 2H $MoTe_2$. *Science* **2021**, *372*, 195–200.
[49] Fraser, J. P.; Masaityte, L.; Zhang, J.; Laing, S.; Moreno-López, J. C.; Mckenzie, A. F.; Mcglynn, J. C.; Panchal, V.; Graham, D.; Kazakova, O.; Pichler, T.; Maclaren, D. A.; Moran, D. a. J.; Ganin, A. Y. Selective phase growth and precise-layer control in $MoTe_2$. *Commun. Mater.* **2020**, *1*, 48–56.
[50] Park, J. C.; Yun, S. J.; Kim, H.; Park, J.-H.; Chae, S. H.; An, S.-J.; Kim, J.-G.; Kim, S. M.; Kim, K. K.; Lee, Y. H. Phase-Engineered Synthesis of Centimeter-Scale 1T'- and 2H-Molybdenum Ditelluride Thin Films. *ACS Nano* **2015**, *9*, 6548–6554.
[51] Wang, X.; Shang, J.; Zhu, M.; Zhou, X.; Hao, R.; Sun, L.; Xu, H.; Zheng, J.; Lei, X.; Li, C.; Kou, L.; Feng, Q. Controlled growth of large-scale uniform 1T' $MoTe_2$ crystals with tunable thickness and their photodetector applications. *Nanoscale Horiz.* **2020**, *5*, 954–959.
[52] Shi, R.; He, P.; Cai, X.; Zhang, Z.; Wang, W.; Wang, J.; Feng, X.; Wu, Z.; Amini, A.; Wang, N.; Cheng, C. Oxide Inhibitor-Assisted Growth of Single-Layer Molybdenum Dichalcogenides ($MoX_2$, X = S, Se, Te) with Controllable Molybdenum Release. *ACS Nano* **2020**, *14*, 7593–7601.
[53] Han, G. H.; Keum, D. H.; Zhao, J.; Shin, B. G.; Song, S.; Bae, J. J.; Lee, J.; Kim, J. H.; Kim, H.; Moon, B. H.; Lee, Y. H. Absorption dichroism of monolayer 1T'-$MoTe_2$ in visible range. *2D Mater.* **2016**, *3*, 031010.
[54] Naylor, C. H.; Parkin, W. M.; Ping, J.; Gao, Z.; Zhou, Y. R.; Kim, Y.; Streller, F.; Carpick, R. W.; Rappe, A. M.; Drndic, M.; Kikkawa, J. M.; Johnson, A. T. Monolayer Single-Crystal 1T'-$MoTe_2$ Grown by Chemical Vapor Deposition Exhibits Weak Antilocalization Effect. *Nano Lett.* **2016**, *16*, 4297–4304.
[55] Xu, X.; Chen, S.; Liu, S.; Cheng, X.; Xu, W.; Li, P.; Wan, Y.; Yang, S.; Gong, W.; Yuan, K.; Gao, P.; Ye, Y.; Dai, L. Millimeter-Scale Single-Crystalline Semiconducting $MoTe_2$ via Solid-to-Solid Phase Transformation. *J. Am. Chem. Soc.* **2019**, *141*, 2128–2134.
[56] Empante, T. A.; Zhou, Y.; Klee, V.; Nguyen, A. E.; Lu, I. H.; Valentin, M. D.; Naghibi Alvillar, S. A.; Preciado, E.; Berges, A. J.; Merida, C. S.; Gomez, M.; Bobek, S.; Isarraraz, M.; Reed, E. J.; Bartels, L. Chemical Vapor Deposition Growth of Few-Layer $MoTe_2$ in the 2H, 1T', and 1T Phases: Tunable Properties of $MoTe_2$ Films. *ACS Nano* **2017**, *11*, 900–905.
[57] Zhang, Q.; Xiao, Y.; Zhang, T.; Weng, Z.; Zeng, M.; Yue, S.; Mendes, R. G.; Wang, L.; Chen, S.; Rümmeli, M. H.; Peng, L.; Fu, L. Iodine-Mediated Chemical Vapor Deposition Growth of Metastable Transition Metal Dichalcogenides. *Chem. Mater.* **2017**, *29*, 4641–4644.
[58] Yoo, Y.; Degregorio, Z. P.; Su, Y.; Koester, S. J.; Johns, J. E. In-Plane 2H-1T' $MoTe_2$ Homojunctions Synthesized by Flux-Controlled Phase Engineering. *Adv. Mater.* **2017**, *29*, 1605461.
[59] Yang, L.; Zhang, W.; Li, J.; Cheng, S.; Xie, Z.; Chang, H. Tellurization Velocity-Dependent Metallic-Semiconducting-Metallic Phase Evolution in Chemical Vapor Deposition Growth of Large-Area, Few-Layer $MoTe_2$. *ACS Nano* **2017**, *11*, 1964–1972.
[60] Zhou, J.; Liu, F.; Lin, J.; Huang, X.; Xia, J.; Zhang, B.; Zeng, Q.; Wang, H.; Zhu, C.; Niu, L.; Wang, X.; Fu, W.; Yu, P.; Chang, T. R.; Hsu, C. H.; Wu, D.; Jeng, H. T.; Huang, Y.; Lin, H.; Shen, Z.; Yang, C.; Lu, L.; Suenaga, K.; Zhou, W.; Pantelides, S. T.; Liu, G.; Liu, Z. Large-Area and High-Quality 2D Transition Metal Telluride. *Adv. Mater.* **2017**, *29*, 1603471.
[61] Chen, K.; Chen, Z.; Wan, X.; Zheng, Z.; Xie, F.; Chen, W.; Gui, X.; Chen, H.; Xie, W.; Xu, J. A Simple Method for Synthesis of High-Quality Millimeter-Scale 1T' Transition-Metal Telluride and Near-Field Nanooptical Properties. *Adv. Mater.* **2017**, *29*, 1700704.
[62] Giri, A.; Yang, H.; Jang, W.; Kwak, J.; Thiyagarajan, K.; Pal, M.; Lee, D.; Singh, R.; Kim, C.; Cho, K. Synthesis of Atomically Thin Transition Metal Ditelluride Films by Rapid Chemical Transformation in Solution Phase. *Chem. Mater.* **2018**, *30*, 2463–2473.
[63] Coleman, J. N.; Lotya, M.; O'neill, A.; Bergin, S. D.; King, P. J.; Khan, U.; Young, K.; Gaucher, A.; De, S.; Smith, R. J.; Shvets, I. V.; Arora, S. K.; Stanton, G.; Kim, H.-Y.; Lee, K.; Kim, G. T.; Duesberg, G. S.; Hallam, T.; Boland, J. J.; Wang, J. J.; Donegan, J. F.; Grunlan, J. C.; Moriarty, G.; Shmeliov, A.; Nicholls, R. J.; Perkins, J. M.; Grieveson, E. M.; Theuwissen, K.; Mccomb, D. W.; Nellist, P. D.; Nicolosi, V. Two-Dimensional Nanosheets Produced by Liquid Exfoliation of Layered

  

Materials. *Science* **2011**, *331*, 568–571.

[64] Dixit, V.; Vyas, C.; Pathak, V. M.; Soalanki, G. K.; Patel, K. D. Structural and optical properties of $WTe_2$ single crystals synthesized by DVT technique. *AIP Conference Proceedings* **2018**, *1953*, 070020.

[65] Jia, Z.-Y.; Song, Y.-H.; Li, X.-B.; Ran, K.; Lu, P.; Zheng, H.-J.; Zhu, X.-Y.; Shi, Z.-Q.; Sun, J.; Wen, J.; Xing, D.; Li, S.-C. Direct visualization of a two-dimensional topological insulator in the single-layer 1T'-$WTe_2$. *Phys. Rev. B* **2017**, *96*, 041108.

[66] Li, J.; Cheng, S.; Liu, Z.; Zhang, W.; Chang, H. Centimeter-Scale, Large-Area, Few-Layer 1T'-$WTe_2$ Films by Chemical Vapor Deposition and Its Long-Term Stability in Ambient Condition. *J. Phys. Chem. C* **2018**, *122*, 7005–7012.

[67] Xiao, Y.; Zhou, M.; Liu, J.; Wei, B.; Yue, S.; Zhou, Y.; Yang, K.; Zhang, T.; Zeng, M.; Wang, Z.; Fu, L. Synthesis of Meta Symmetric 1T'-$WTe_2$ Using an Edge-Induced Mechanism. *Chin. J. Chem.* **2020**, *38*, 709–713.

[68] Zhou, Y.; Jang, H.; Woods, J. M.; Xie, Y.; Kumaravadivel, P.; Pan, G. A.; Liu, J.; Liu, Y.; Cahill, D. G.; Cha, J. J. Direct Synthesis of Large-Scale $WTe_2$ Thin Films with Low Thermal Conductivity. *Adv. Funct. Mater.* **2017**, *27*, 1605928.

[69] Sun, Y.; Fujisawa, K.; Terrones, M.; Schaak, R. E. Solution synthesis of few-layer $WTe_2$ and $Mo_xW_{1-x}Te_2$ nanostructures. *J. Mater. Chem. C* **2017**, *5*, 11317–11323.

[70] Yin, G.; Zhu, D.; Lv, D.; Hashemi, A.; Fei, Z.; Lin, F.; Krasheninnikov, A. V.; Zhang, Z.; Komsa, H. P.; Jin, C. Hydrogen-assisted post-growth substitution of tellurium into molybdenum disulfide monolayers with tunable compositions. *Nanotechnology* **2018**, *29*, 145603.

[71] Yun, S. J.; Han, G. H.; Kim, H.; Duong, D. L.; Shin, B. G.; Zhao, J.; Vu, Q. A.; Lee, J.; Lee, S. M.; Lee, Y. H. Telluriding monolayer $MoS_2$ and $WS_2$ via alkali metal scooter. *Nat. Commun.* **2017**, *8*, 2163.

[72] Lin, J.; Zhou, J.; Zuluaga, S.; Yu, P.; Gu, M.; Liu, Z.; Pantelides, S. T.; Suenaga, K. Anisotropic Ordering in 1T' Molybdenum and Tungsten Ditelluride Layers Alloyed with Sulfur and Selenium. *ACS Nano* **2018**, *12*, 894–901.

[73] Kim, D.; Oh, G. H.; Kim, A.; Shin, C.; Park, J.; Kim, S. I.; Kim, T. Atomic Layer $MoS_{2x}Te_{2(1-x)}$ Ternary Alloys: Two-Dimensional van der Waals Growth, Band gap Engineering, and Electrical Transport. *ACS Appl. Mater. Inter.* **2020**, *12*, 40518–40524.

[74] Zhao, S.; Lu, M.; Xue, S.; Tao, L.; Sui, Y.; Wang, Y. Large-area synthesis of monolayer $MoTe_xSe_{2-x}$ alloys by chemical vapor deposition. *Appl. Phys. Lett.* **2019**, *115*, 063105.

[75] Li, P.; Cui, J.; Zhou, J.; Guo, D.; Zhao, Z.; Yi, J.; Fan, J.; Ji, Z.; Jing, X.; Qu, F.; Yang, C.; Lu, L.; Lin, J.; Liu, Z.; Liu, G. Phase Transition and Superconductivity Enhancement in Se-Substituted $MoTe_2$ Thin Films. *Adv. Mater.* **2019**, *31*, 04641.

[76] Apte, A.; Krishnamoorthy, A.; Hachtel, J. A.; Susarla, S.; Idrobo, J. C.; Nakano, A.; Kalia, R. K.; Vashishta, P.; Tiwary, C. S.; Ajayan, P. M. Telluride-Based Atomically Thin Layers of Ternary Two-Dimensional Transition Metal Dichalcogenide Alloys. *Chem. Mater.* **2018**, *30*, 7262–7268.

[77] Diaz, H. C.; Ma, Y.; Kolekar, S.; Avila, J.; Chen, C.; Asensio, M. C.; Batzill, M. Substrate dependent electronic structure variations of van der Waals heterostructures of $MoSe_2$ or $MoSe_{2(1-x)}Te_{2x}$ grown by van der Waals epitaxy. *2D Mater.* **2017**, *4*, 025094.

[78] Wang, Z.; Sun, J.; Wang, H.; Lei, Y.; Xie, Y.; Wang, G.; Zhao, Y.; Li, X.; Xu, H.; Yang, X.; Feng, L.; Ma, X. 2H/1T' phase $WS_{2(1-x)}Te_{2x}$ alloys grown by chemical vapor deposition with tunable band structures. *Appl. Surf. Sci.* **2020**, *504*, 144371.

[79] Tang, B.; Zhou, J.; Sun, P.; Wang, X.; Bai, L.; Dan, J.; Yang, J.; Zhou, K.; Zhao, X.; Pennycook, S. J.; Liu, Z. Phase-Controlled Synthesis of Monolayer Ternary Telluride with a Random Local Displacement of Tellurium Atoms. *Adv. Mater.* **2019**, *31*, 1900862.

[80] Oliver, S. M.; Young, J.; Krylyuk, S.; Reinecke, T. L.; Davydov, A. V.; Vora, P. M. Valley phenomena in the candidate phase change material $WSe_{2(1-x)}Te_{2x}$. *Commun. Phys.* **2020**, *3*, 10.

[81] Yu, P.; Lin, J.; Sun, L.; Le, Q. L.; Yu, X.; Gao, G.; Hsu, C. H.; Wu, D.; Chang, T. R.; Zeng, Q.; Liu, F.; Wang, Q. J.; Jeng, H. T.; Lin, H.; Trampert, A.; Shen, Z.; Suenaga, K.; Liu, Z. Metal-Semiconductor Phase-Transition in $WSe_{2(1-x)}$ $Te_{2x}$ Monolayer. *Adv. Mater.* **2017**, *29*, 1603991.

[82] Barton, A. T.; Yue, R.; Walsh, L. A.; Zhou, G.; Cormier, C.; Smyth, C. M.; Addou, R.; Colombo, L.; Wallace, R. M.; Hinkle, C. L. $WSe_{(2-x)}Te_x$ alloys grown by molecular beam epitaxy. *2D Mater.* **2019**, *6*, 045027.

[83] Oliver, S.; Beams, R.; Krylyuk, S.; Kalish, I.; Singh, A.; Bruma, A.; Tavazza, F.; Joshi, J.; Stone, I.; Stranick, S. The structural phases and vibrational properties of $Mo_{1-x}W_xTe_2$ alloys. *2D Mater.* **2017**, *4*, 045008.

[84] Rhodes, D.; Chenet, D. A.; Janicek, B. E.; Nyby, C.; Lin, Y.; Jin, W.; Edelberg, D.; Mannebach, E.; Finney, N.; Antony, A.; Schiros, T.; Klarr, T.; Mazzoni, A.; Chin, M.; Chiu, Y. C.; Zheng, W.; Zhang, Q. R.; Ernst, F.; Dadayp, J. I.; Tong, X.; Ma, J.; Lou, R.; Wan, S.; Qian, T.; Ding, H.; Osgood, R. M., Jr.; Paley, D. W.; Lindenberg, A. M.; Huang, P. Y.; Pasupathy, A. N.; Dubey, M.; Hone, J.; Balicas, L. Engineering the Structural and Electronic Phases of $MoTe_2$ through W Substitution. *Nano Lett.* **2017**, *17*, 1616–1622.

[85] Lv, Y.-Y.; Zhang, B.-B.; Li, X.; Pang, B.; Zhang, F.; Lin, D.-J.; Zhou, J.; Yao, S.-H.; Chen, Y. B.; Zhang, S.-T.; Lu, M.; Liu, Z.; Chen, Y.; Chen, Y.-F. Dramatically decreased magnetoresistance in non-stoichiometric $WTe_2$ crystals. *Sci. Rep.* **2016**, *6*, 26903.

[86] Liu, S.-J.; Zou, Y.-C.; Shi, X.-L.; Li, Q.-Z.; Yang, Y.-Z.; Liu, W.-D.; Chen, Z.-G.; Zou, J. Vapour-solid growth of $Mo_xW_{1-x}Te_2$ nanobelts by a facile chemical vapour deposition method. *J. Alloys Compd.* **2019**, *777*, 926–930.

[87] Mathew, R. J.; Lee, C. P.; Tseng, C. A.; Chand, P. K.; Huang, Y. J.; Chen, H. T.; Ho, K. C.; Anbalagan, A. K.; Lee, C. H.; Chen, Y. T. Stoichiometry-Controlled $Mo_xW_{1-x}Te_2$ Nanowhiskers: A Novel Electrocatalyst for Pt-Free Dye-Sensitized Solar Cells. *ACS Appl. Mater. Inter.* **2020**, *12*, 34815–34824.

[88] Hudie, S. M.; Lee, C.-P.; Mathew, R. J.; Chien, T.-E.; Huang, Y.-J.; Chen, H.-T.; Ho, K.-C.; Tseng, C.-A.; Chen, Y.-T. Phase-Engineered Weyl Semi-Metallic $Mo_xW_{1-x}Te_2$ Nanosheets as a Highly Efficient Electrocatalyst for Dye-Sensitized Solar Cells. *Solar RRL* **2019**, *3*, 1800314.

[89] Mathew, R. J.; Inbaraj, C. R. P.; Sankar, R.; Hudie, S. M.; Nikam, R. D.; Tseng, C.-A.; Lee, C.-H.; Chen, Y.-T. High unsaturated room-temperature magnetoresistance in phase-engineered $Mo_xW_{1-x}Te_{2+\delta}$ ultrathin films. *J. Mater. Chem. C* **2019**, *7*, 10996–11004.

[90] Huang, Y.; Pan, Y. H.; Yang, R.; Bao, L. H.; Meng, L.; Luo, H. L.; Cai, Y. Q.; Liu, G. D.; Zhao, W. J.; Zhou, Z.; Wu, L. M.; Zhu, Z. L.; Huang, M.; Liu, L. W.; Liu, L.; Cheng, P.; Wu, K. H.; Tian, S. B.; Gu, C. Z.; Shi, Y. G.; Guo, Y. F.; Cheng, Z. G.; Hu, J. P.; Zhao, L.; Yang, G. H.; Sutter, E.; Sutter, P.; Wang, Y. L.; Ji, W.; Zhou, X. J.; Gao, H. J. Universal mechanical exfoliation of large-area 2D crystals. *Nat. Commun.* **2020**, *11*, 2453.

[91] Shim, J.; Bae, S. H.; Kong, W.; Lee, D.; Qiao, K.; Nezich, D.; Park, Y. J.; Zhao, R.; Sundaram, S.; Li, X. Controlled crack propagation for atomic precision handling of wafer-scale two-dimensional materials. *Science* **2018**, *362*, 665–670.

[92] Desai, S. B.; Madhvapathy, S. R.; Amani, M.; Kiriya, D.; Javey, A. Gold-Mediated Exfoliation of Ultralarge Optoelectronically-Perfect Monolayers. *Adv. Mater.* **2016**, *28*, 4053–4058.

[93] Velicky, M.; Donnelly, G. E.; Hendren, W. R.; Mcfarland, S.; Scullion, D.; Debenedetti, W. J. I.; Correa, G. C.; Han, Y.; Wain, A. J.; Hines, M. A.; Muller, D. A.; Novoselov, K. S.; Abruna, H. D.; Bowman, R. M.; Santos, E. J. G.; Huang, F. Mechanism of Gold-Assisted Exfoliation of Centimeter-Sized Transition-Metal Dichalcogenide Monolayers. *ACS Nano* **2018**, *12*, 10463–10472.

[94] Magda, G. Z.; Peto, J.; Dobrik, G.; Hwang, C.; Biro, L. P.; Tapaszto, L. Exfoliation of large-area transition metal chalcogenide single layers. *Sci. Rep.* **2015**, *5*, 14714.

[95] Cohen, A.; Patsha, A.; Mohapatra, P. K.; Kazes, M.; Ranganathan, K.; Houben, L.; Oron, D.; Ismach, A. Growth-Etch Metal-Organic Chemical Vapor Deposition Approach of $WS_2$ Atomic Layers. *ACS Nano* **2021**, *15*, 526–538.

[96] Ma, J.; Tang, K.; Mao, H.; Ye, J.; Zhu, S.; Xu, Z.; Yao, Z.; Gu, S.; Zheng, Y. Behavior and impact of sulfur incorporation in Zinc Oxysulfide alloy grown by metal organic chemical vapor deposition. *Appl. Surf. Sci.*

  

**2018**, *435*, 297–304.

[97] Zhou, L.; Xu, K.; Zubair, A.; Zhang, X.; Ouyang, F.; Palacios, T.; Dresselhaus, M. S.; Li, Y.; Kong, J. Role of Molecular Sieves in the CVD Synthesis of Large-Area 2D $MoTe_2$. *Adv. Funct. Mater.* **2017**, *27*, 1603491.

[98] Shi, R.; He, P.; Cai, X.; Zhang, Z.; Cheng, C. Oxide Inhibitor-Assisted Growth of Single-Layer Molybdenum Dichalcogenides ($MoX_2$, X=S, Se, Te) with Controllable Molybdenum Release. *ACS Nano* **2020**, *14*, 7593–7601.

[99] Zhou, J.; Lin, J.; Huang, X.; Zhou, Y.; Chen, Y.; Xia, J.; Wang, H.; Xie, Y.; Yu, H.; Lei, J.; Wu, D.; Liu, F.; Fu, Q.; Zeng, Q.; Hsu, C. H.; Yang, C.; Lu, L.; Yu, T.; Shen, Z.; Lin, H.; Yakobson, B. I.; Liu, Q.; Suenaga, K.; Liu, G.; Liu, Z. A library of atomically thin metal chalcogenides. *Nature* **2018**, *556*, 355–359.

[100] Li, X.; Kahn, E.; Chen, G.; Sang, X.; Lei, J.; Passarello, D.; Oyedele, A. D.; Zakhidov, D.; Chen, K.-W.; Chen, Y.-X.; Hsieh, S.-H.; Fujisawa, K.; Unocic, R. R.; Xiao, K.; Salleo, A.; Toney, M. F.; Chen, C.-H.; Kaxiras, E.; Terrones, M.; Yakobson, B. I.; Harutyunyan, A. R. Surfactant-Mediated Growth and Patterning of Atomically Thin Transition Metal Dichalcogenides. *ACS Nano* **2020**, *14*, 6570–6581.

[101] Song, J. G.; Hee Ryu, G.; Kim, Y.; Je Woo, W.; Yong Ko, K.; Kim, Y.; Lee, C.; Oh, I. K.; Park, J.; Lee, Z.; Kim, H. Catalytic chemical vapor deposition of large-area uniform two-dimensional molybdenum disulfide using sodium chloride. *Nanotechnology* **2017**, *28*, 465103.

[102] Yang, P.; Zou, X.; Zhang, Z.; Hong, M.; Shi, J.; Chen, S.; Shu, J.; Zhao, L.; Jiang, S.; Zhou, X.; Huan, Y.; Xie, C.; Gao, P.; Chen, Q.; Zhang, Q.; Liu, Z.; Zhang, Y. Batch production of 6-inch uniform monolayer molybdenum disulfide catalyzed by sodium in glass. *Nat. Commun.* **2018**, *9*, 979.

[103] Ji, Q.; Su, C.; Mao, N.; Tian, X.; Idrobo, J.-C.; Miao, J.; Tisdale, W. A.; Zettl, A.; Li, J.; Kong, J. Revealing the Bronsted-Evans-Polanyi relation in halide-activated fast $MoS_2$ growth toward millimeter-sized 2D crystals. *Sci. Adv.* **2021**, *7*, eabj3274.

[104] Li, W.; Huang, J.; Han, B.; Xie, C.; Huang, X.; Tian, K.; Zeng, Y.; Zhao, Z.; Gao, P.; Zhang, Y.; Yang, T.; Zhang, Z.; Sun, S.; Hou, Y. Molten-Salt-Assisted Chemical Vapor Deposition Process for Substitutional Doping of Monolayer $MoS_2$ and Effectively Altering the Electronic Structure and Phononic Properties. *Adv. Sci.* **2020**, *7*, 2001080.

[105] Zhou, L.; Zubair, A.; Wang, Z.; Zhang, X.; Ouyang, F.; Xu, K.; Fang, W.; Ueno, K.; Li, J.; Palacios, T.; Kong, J.; Dresselhaus, M. S. Synthesis of High-Quality Large-Area Homogenous 1T' $MoTe_2$ from Chemical Vapor Deposition. *Adv. Mater.* **2016**, *28*, 9526–9531.

[106] Lin, J.; Zhou, J.; Zuluaga, S.; Yu, P.; Gu, M.; Liu, Z.; Pantelides, S. T.; Suenaga, K. Anisotropic Ordering in 1T ' Molybdenum and Tungsten Ditelluride Layers Alloyed with Sulfur and Selenium. *ACS Nano* **2018**, *12*, 894–901.

[107] Burton, B. P.; Sluiter, M. H. F. First principles phase diagram calculation for the 2D TMD system $WS_2$-$WTe_2$. *Calphad* **2018**, *63*, 142–147.

[108] Liu, L.; Wu, J.; Wu, L.; Ye, M.; Liu, X.; Wang, Q.; Hou, S.; Lu, P.; Sun, L.; Zheng, J.; Xing, L.; Gu, L.; Jiang, X.; Xie, L.; Jiao, L. Phase-selective synthesis of 1T′ $MoS_2$ monolayers and heterophase bilayers. *Nat. Mater.* **2018**, *17*, 1108–1114.

[109] Giri, A.; Park, G.; Yang, H.; Pal, M.; Kwak, J.; Jeong, U. Synthesis of 2D Metal Chalcogenide Thin Films through the Process Involving Solution-Phase Deposition. *Adv. Mater.* **2018**, *30*, e1707577.

[110] Cheon, Y.; Lim, S. Y.; Kim, K.; Cheong, H. Structural Phase Transition and Interlayer Coupling in Few-Layer 1T' and $T_d$ $MoTe_2$. *ACS Nano* **2021**, *15*, 2962–2970.

[111] Cho, S.; Kim, S.; Kim, J. H.; Zhao, J.; Seok, J.; Keum, D. H.; Baik, J.; Choe, D. H.; Chang, K. J.; Suenaga, K. Phase patterning for ohmic homojunction contact in $MoTe_2$. *Science* **2015**, *349*, 625–628.

[112] Zhang, C.; Kc, S.; Nie, Y.; Liang, C.; Vandenberghe, W. G.; Longo, R. C.; Zheng, Y.; Kong, F.; Hong, S.; Wallace, R. M.; Cho, K. Charge Mediated Reversible Metal-Insulator Transition in Monolayer $MoTe_2$ and $W_xMo_{1-x}Te_2$ Alloy. *ACS Nano* **2016**, *10*, 7370–7375.

[113] Zhang, K.; Bao, C.; Gu, Q.; Ren, X.; Zhang, H.; Deng, K.; Wu, Y.; Li, Y.; Feng, J.; Zhou, S. Raman signatures of inversion symmetry breaking and structural phase transition in type-II Weyl semimetal $MoTe_2$. *Nat. Commun.* **2016**, *7*, 13552.

[114] Cao, C.; Liu, X.; Ren, X.; Zeng, X.; Zhang, K.; Sun, D.; Zhou, S.; Wu, Y.; Li, Y.; Chen, J.-H. Barkhausen effect in the first order structural phase transition in type-II Weyl semimetal $MoTe_2$. *2D Mater.* **2018**, *5*, 044003.

[115] Berkdemir, A.; Gutiérrez, H.; Botello-Méndez, A.; Perea-López, N.; Elías, A.; Chia, C. I.; Wang, B.; Crespi, V. H.; López-Urías, F.; Charlier, J. C. Identification of individual and few layers of $WS_2$ using Raman spectroscopy. *Sci. Rep.* **2013**, *3*, 1755.

[116] Gaur, A.; Sahoo, S.; Scott, J. F.; Katiyar, R. S. Electron–Phonon Interaction and Double-Resonance Raman Studies in Monolayer $WS_2$. *J. Phys. Chem. C* **2016**, *119*, 5146–5151.

[117] Bie, Y.-Q.; Grosso, G.; Heuck, M.; Furchi, M. M.; Cao, Y.; Zheng, J.; Bunandar, D.; Navarro-Moratalla, E.; Zhou, L.; Efetov, D. K. A $MoTe_2$-based light-emitting diode and photodetector for silicon photonic integrated circuits. *Nat. Nanotechnol.* **2017**, *12*, 1124–1129.

[118] Yang, D.; Hu, X.; Zhuang, M.; Ding, Y.; Zhou, S.; Li, A.; Yu, Y.; Li, H.; Luo, Z.; Gan, L. Inversion Symmetry Broken 2D 3R-$MoTe_2$. *Adv. Funct. Mater.* **2018**, *28*, 1800785.

[119] Cheng, R.; Wang, F.; Yin, L.; Wang, Z.; Wen, Y.; Shifa, T. A.; He, J. High-performance, multifunctional devices based on asymmetric van der Waals heterostructures. *Nat. Electron.* **2018**, *1*, 356–361.

[120] Zhu, Y.; Li, Z.; Zhang, L.; Wang, B.; Luo, Z.; Long, J.; Yang, J.; Fu, L.; Lu, Y. High-efficiency monolayer molybdenum ditelluride light-emitting diode and photodetector. *ACS Appl. Mater. Interfaces* **2018**, *10*, 43291–43298.

[121] Zhou, W.; Chen, J.; Gao, H.; Hu, T.; Ruan, S.; Stroppa, A.; Ren, W. Anomalous and Polarization-Sensitive Photoresponse of $T_d$-$WTe_2$ from Visible to Infrared Light. *Adv. Mater.* **2019**, *31*, 1804629.

[122] Chen, M.; Lee, K.; Li, J.; Cheng, L.; Wang, Q.; Cai, K.; Chia, E. E.; Chang, H.; Yang, H. Anisotropic picosecond spin-photocurrent from Weyl semimetal $WTe_2$. *ACS Nano* **2020**, *14*, 3539–3545.

[123] Wang, Y.; Liu, E.; Liu, H.; Pan, Y.; Zhang, L.; Zeng, J.; Fu, Y.; Wang, M.; Xu, K.; Huang, Z.; Wang, Z.; Lu, H.-Z.; Xing, D.; Wang, B.; Wan, X.; Miao, F. Gate-tunable negative longitudinal magnetoresistance in the predicted type-II Weyl semimetal $WTe_2$. *Nat. Commun.* **2016**, *7*, 13142.

[124] Huang, X.; Zhao, L.; Long, Y.; Wang, P.; Chen, D.; Yang, Z.; Liang, H.; Xue, M.; Weng, H.; Fang, Z.; Dai, X.; Chen, G. Observation of the Chiral-Anomaly-Induced Negative Magnetoresistance in 3D Weyl Semimetal TaAs. *Phys. Rev. X* **2015**, *5*, 031023.

[125] Son, D. T.; Spivak, B. Z. Chiral anomaly and classical negative magnetoresistance of Weyl metals. *Phys. Rev. B* **2013**, *88*, 104412.

[126] Zhang, C.-L.; Xu, S.-Y.; Belopolski, I.; Yuan, Z.; Lin, Z.; Tong, B.; Bian, G.; Alidoust, N.; Lee, C.-C.; Huang, S.-M.; Chang, T.-R.; Chang, G.; Hsu, C.-H.; Jeng, H.-T.; Neupane, M.; Sanchez, D. S.; Zheng, H.; Wang, J.; Lin, H.; Zhang, C.; Lu, H.-Z.; Shen, S.-Q.; Neupert, T.; Hasan, M. Z.; Jia, S. Signatures of the Adler-Bell-Jackiw chiral anomaly in a Weyl fermion semimetal. *Nat. Commun.* **2016**, *7*, 10735.

[127] Li, P.; Wen, Y.; He, X.; Zhang, Q.; Xia, C.; Yu, Z.-M.; Yang, S. A.; Zhu, Z.; Alshareef, H. N.; Zhang, X.-X. Evidence for topological type-II Weyl semimetal $WTe_2$. *Nat. Commun.* **2017**, *8*, 2150.

[128] Hikami, S.; Larkin, A. I.; Nagaoka, Y. Spin-orbit interaction and magnetoresistance in the 2 dimensional random system. *Prog. Theor. Phys.* **1980**, *63*, 707–710.

[129] Wang, Q.; Yu, P.; Huang, X.; Fan, J.; Jing, X.; Ji, Z.; Liu, Z.; Liu, G.; Yang, C.; Lu, L. Observation of Weak Anti-Localization and Electron-Electron Interaction on Few-Layer 1T '-$MoTe_2$ Thin Films. *Chin. Phys. Lett.* **2018**, *35*, 077303.

[130] Wang, L.; Gutierrez-Lezama, I.; Barreteau, C.; Ubrig, N.; Giannini, E.; Morpurgo, A. F. Tuning Magnetotransport in a Compensated Semimetal at the Atomic Scale. *Nat. Commun.* **2015**, *6*, 8892.

[131] Kang, D.; Zhou, Y.; Yi, W.; Yang, C.; Guo, J.; Shi, Y.; Zhang, S.; Wang, Z.; Zhang, C.; Jiang, S.; Li, A.; Yang, K.; Wu, Q.; Zhang, G.; Sun, L.; Zhao, Z. Superconductivity emerging from a suppressed large magnetoresistant state in tungsten ditelluride. *Nat. Commun.* **2015**, *6*, 7804.

  

[132] Li, Q.; He, C.; Wang, Y.; Liu, E.; Wang, M.; Wang, Y.; Zeng, J.; Ma, Z.; Cao, T.; Yi, C. Proximity-Induced Superconductivity with Subgap Anomaly in Type II Weyl Semi-Metal $WTe_2$. *Nano Lett.* **2018**, *18*, 7962–7968.

[133] Tsen, A. W.; Hunt, B.; Kim, Y. D.; Yuan, Z. J.; Jia, S.; Cava, R. J.; Hone, J.; Kim, P.; Dean, C. R.; Pasupathy, A. N. Nature of the quantum metal in a two-dimensional crystalline superconductor. *Nat. Phys.* **2016**, *12*, 208–212.

[134] Xu, C.; Wang, L.; Liu, Z.; Chen, L.; Guo, J.; Kang, N.; Ma, X.-L.; Cheng, H.-M.; Ren, W. Large-area high-quality 2D ultrathin $Mo_2C$ superconducting crystals. *Nat. Mater.* **2015**, *14*, 1135–1141.

[135] Cui, J.; Li, P.; Zhou, J.; He, W.-Y.; Huang, X.; Yi, J.; Fan, J.; Ji, Z.; Jing, X.; Qu, F.; Cheng, Z. G.; Yang, C.; Lu, L.; Suenaga, K.; Liu, J.; Law, K. T.; Lin, J.; Liu, Z.; Liu, G. Transport evidence of asymmetric spin–orbit coupling in few-layer superconducting $1T_d$-$MoTe_2$. *Nat. Commun.* **2019**, *10*, 2044.

[136] Dynes, R. C. Mcmillans Equation and $T_c$ of Superconductors. *Solid State Commun.* **1972**, *10*, 615–618.

[137] Zhu, L.; Li, Q.-Y.; Lv, Y.-Y.; Li, S.; Zhu, X.-Y.; Jia, Z.-Y.; Chen, Y. B.; Wen, J.; Li, S.-C. Superconductivity in Potassium-intercalated $T_d$-$WTe_2$. *Nano Lett.* **2018**, *18*, 6585–6590.

[138] Chen, F. C.; Luo, X.; Xiao, R. C.; Lu, W. J.; Zhang, B.; Yang, H. X.; Li, J. Q.; Pei, Q. L.; Shao, D. F.; Zhang, R. R.; Ling, L. S.; Xi, C. Y.; Song, W. H.; Sun, Y. P. Superconductivity enhancement in the S-doped Weyl semimetal candidate $MoTe_2$. *Appl. Phys. Lett.* **2016**, *108*, 162601.

[139] Song, T.; Cai, X.; Tu, W. Y.; Zhang, X.; Huang, B.; Wilson, N. P.; Seyler, K. L.; Zhu, L.; Taniguchi, T.; Watanabe, K. Giant Tunneling Magnetoresistance in Spin-Filter van der Waals Heterostructures. *Science* **2018**, *360*, 1214–1218.

[140] Seyler, K.; Zhong, D.; Huang, B.; Linpeng, X.; Wilson, N. P.; Taniguchi, T.; Watanabe, K.; Yao, W.; Xiao, D.; Mcguire, M. A. Valley Manipulation by Optically Tuning the Magnetic Proximity Effect in $WSe_2/CrI_3$ Heterostructures. *Nano Lett.* **2018**, *18*, 3823–3828.

[141] Huang, B.; Clark, G.; Klein, D. R.; Macneill, D.; Navarro-Moratalla, E.; Seyler, K. L.; Wilson, N.; Mcguire, M. A.; Cobden, D. H.; Xiao, D. Electrical control of 2D magnetism in bilayer CrI. *Nat. Nanotechnol.* **2018**, *13*, 544–548.

[142] Chang, C. Z.; Zhang, J.; Feng, X.; Shen, J.; Xue, Q. K. Experimental Observation of the Quantum Anomalous Hall Effect in a Magnetic Topological Insulator. *Science* **2013**, *340*, 167–170.

[143] Noam; Morali; Rajib; Batabyal; Pranab; Kumar; Nag; Enke; Liu; Qiunan. Fermi-arc diversity on surface terminations of the magnetic Weyl semimetal $Co_3Sn_3S_2$. *Science* **2019**, *365*, 1286–1291.

[144] Qi, W.; Yuanfeng, X.; Rui, L.; Zhonghao, L.; Man, L. Large intrinsic anomalous Hall effect in half-metallic ferromagnet $Co_3Sn_2S_2$ with magnetic Weyl fermions. *Nat. Commun.* **2018**, *9*, 3681.

[145] Xu, Q.; Liu, E.; Shi, W.; Muechler, L.; Gayles, J.; Felser, C.; Sun, Y. Topological surface Fermi arcs in the magnetic Weyl semimetal $Co_3Sn_2S_2$. *Phys. Rev. B* **2018**, *97*, 235416.

[146] Liu, E.; Yan, S.; Nitesh, K.; Lukas, M.; Sun, A.; Jiao, L.; Yang, S. Y.; Liu, D.; Liang, A.; Xu, Q. Giant anomalous Hall effect in a ferromagnetic Kagomé-lattice semimetal. *Nat. Phys.* **2018**, *14*, 1125–1131.

[147] Gronvold, F.; Westrum, E. Thermodynamic Aspects of the Magnetic Transitions in the Chromium Tellurides-Heat Capacities of $CR_5TE_6$, $CR_3TE_4$ and $CR_2TE_3$ from 5 K to 350 K. *Z. Anorg. Allg. Chem.* **1964**, *328*, 272–282.

[148] Wen, Y.; Liu, Z.; Zhang, Y.; Xia, C.; Zhai, B.; Zhang, X.; Zhai, G.; Shen, C.; He, P.; Cheng, R.; Yin, L.; Yao, Y.; Getaye Sendeku, M.; Wang, Z.; Ye, X.; Liu, C.; Jiang, C.; Shan, C.; Long, Y.; He, J. Tunable Room-Temperature Ferromagnetism in Two-Dimensional $Cr_2Te_3$. *Nano Lett.* **2020**, *20*, 3130–3139.

[149] Zhi, W.; Zhang, T.; Mei, D.; Dong, B.; Li, Y.; Chen, M.; Li, X.; Huang, J.; Wang, H.; Zhao, X. Electric-field control of magnetism in a few-layered van der Waals ferromagnetic semiconductor. *Nat. Nanotechnol.* **2018**, *13*, 554–559.

[150] Lin, Y.; Xu, Y.; Wang, S.; Li, S.; Yamamoto, M.; Aparecido-Ferreira, A.; Li, W.; Sun, H.; Nakaharai, S.; Jian, W. Ambipolar $MoTe_2$ Transistors and Their Applications in Logic Circuits. *Adv. Mater.* **2014**, *26*, 3263–3269.

[151] Guo, H.; Zhu, W.; Rehman, Z. U.; Wu, C.; Chen, S.; Song, L. Ternary $MoSe_{2x}Te_{2-2x}$ alloy with tunable band gap for electronic and optoelectronic transistors. *Nanotechnology* **2020**, *31*, 345704.

[152] Wang, F.; Tu, B.; He, P.; Wang, Z.; Yin, L.; Cheng, R.; Wang, J.; Fang, Q.; He, J. Uncovering the Conduction Behavior of van der Waals Ambipolar Semiconductors. *Adv. Mater.* **2019**, *31*, 1805317.

[153] Liu, J.; Liu, X.; Chen, Z.; Miao, L.; Liu, X.; Li, B.; Tang, L.; Chen, K.; Liu, Y.; Li, J.; Wei, Z.; Duan, X. Tunable Schottky barrier width and enormously enhanced photoresponsivity in Sb doped $SnS_2$ monolayer. *Nano Res.* **2019**, *12*, 463–468.

[154] Knoch, J.; Zhang, M.; Appenzeller, J.; Mantl, S. Physics of ultrathin-body silicon-on-insulator Schottky-barrier field-effect transistors. *Appl. Phys. A* **2007**, *87*, 351–357.

[155] Penumatcha, A. V.; Salazar, R. B.; Appenzeller, J. Analysing black phosphorus transistors using an analytic Schottky barrier MOSFET model. *Nat. Commun.* **2015**, *6*, 8948.

[156] Das, S.; Appenzeller, J. $WSe_2$ field effect transistors with enhanced ambipolar characteristics. *Appl. Phys. Lett.* **2013**, *103*, 4820408.

[157] Wuttig, M.; Bhaskaran, H.; Taubner, T. Phase-change materials for non-volatile photonic applications. *Nat. Photonics* **2017**, *11*, 465–476.

[158] Shi, S.; Liang, S.; Zhu, Z.; Cai, K.; Pollard, S. D.; Wang, Y.; Wang, J.; Wang, Q.; He, P.; Yu, J.; Eda, G.; Liang, G.; Yang, H. All-electric magnetization switching and Dzyaloshinskii-Moriya interaction in $WTe_2$/ferromagnet heterostructures. *Nat. Nanotechnol.* **2019**, *14*, 945–949.

[159] Liu, Y.; Shao, A. Two-Dimensional Materials for Energy-Efficient Spin-Orbit Torque Devices. *ACS Nano* **2020**, *14*, 9389–9407.

[160] Zhao, B.; Karpiak, B.; Khokhriakov, D.; Johansson, A.; Hoque, A. M.; Xu, X.; Jiang, Y.; Mertig, I.; Dash, S. P. Unconventional Charge-Spin Conversion in Weyl-Semimetal $WTe_2$. *Adv. Mater.* **2020**, *32*, 2000818.

[161] Zhao, B.; Hoque, A. M.; Khokhriakov, D.; Karpiak, B.; Dash, S. P. Charge-spin conversion signal in $WTe_2$ van der Waals hybrid devices with a geometrical design. *Appl. Phys. Lett.* **2020**, *117*, 0029071.

[162] Xu, S. Y.; Alidoust, N.; Belopolski, I.; Yuan, Z.; Bian, G.; Chang, T. R.; Zheng, H.; Strocov, V. N.; Sanchez, D. S.; Chang, G. Discovery of a Weyl fermion state with Fermi arcs in niobium arsenide. *Nat. Phys.* **2015**, *11*, 748–754.

[163] Yang, L.; Liu, Z.; Sun, Y.; Peng, H.; Yang, H.; Zhang, T.; Zhou, B.; Zhang, Y.; Guo, Y.; Rahn, M. Discovery of a Weyl Semimetal in non-Centrosymmetric Compound TaAs. *Nat. Phys.* **2015**, *11*, 728–732.

[164] Weng, H.; Fang, C.; Fang, Z.; Bernevig, B. A.; Dai, X. Weyl Semimetal Phase in Noncentrosymmetric Transition-Metal Monophosphides. *Phys. Rev. X* **2015**, *5*, 011029.

[165] Shuang, J.; Xu, S. Y.; Hasan, M. Z. Weyl semimetals, Fermi arcs and chiral anomalies. *Nat. Mater.* **2016**, *15*, 1140–1144.

[166] Huang, L.; Mccormick, T. M.; Ochi, M.; Zhao, Z.; Suzuki, M. T.; Arita, R.; Yun, W.; Mou, D.; Cao, H.; Yan, J. Spectroscopic evidence for a type II Weyl semimetallic state in $MoTe_2$. *Nat. Mater.* **2016**, *15*, 1155–1160.

[167] Liang, T.; Gibson, Q.; Ali, M. N.; Liu, M.; Cava, R. J.; Ong, N. P. Ultrahigh mobility and giant magnetoresistance in the Dirac semimetal $Cd_3As_2$. *Nat. Mater.* **2015**, *14*, 280–284.

[168] Shekhar, C.; Nayak, A. K.; Sun, Y.; Schmidt, M.; Nicklas, M.; Leermakers, I.; Zeitler, U.; Skourski, Y.; Wosnitza, J.; Liu, Z.; Chen, Y.; Schnelle, W.; Borrmann, H.; Grin, Y.; Felser, C.; Yan, B. Extremely large magnetoresistance and ultrahigh mobility in the topological Weyl semimetal candidate NbP. *Nat. Phys.* **2015**, *11*, 645–649.

[169] Wan, X.; Turner, A. M.; Vishwanath, A.; Savrasov, S. Y. Topological semimetal and Fermi-arc surface states in the electronic structure of pyrochlore iridates. *Phys. Rev. B* **2011**, *83*, 205101.

[170] Rajamathi, C. R.; Gupta, U.; Kumar, N.; Yang, H.; Sun, Y.; Suess, V.; Shekhar, C.; Schmidt, M.; Blumtritt, H.; Werner, P.; Yan, B.; Parkin, S.; Felser, C.; Rao, C. N. R. Weyl Semimetals as Hydrogen Evolution Catalysts. *Adv. Mater.* **2017**, *29*, 1606202.


  

[171] Hosur, P.; Qi, X. Recent developments in transport phenomena in Weyl semimetals. *C. R. Phys.* **2013**, *14*, 857–870.
[172] Politano, A.; Chiarello, G.; Li, Z.; Fabio, V.; Wang, L.; Guo, L.; Chen, X.; Boukhvalov, D. W. Toward the Effective Exploitation of Topological Phases of Matter in Catalysis: Chemical Reactions at the Surfaces of NbAs and TaAs Weyl Semimetals. *Adv. Funct. Mater.* **2018**, *28*, 1800511.
[173] Hasan, M. Z.; Kane, C. L. Colloquium: Topological insulators. *Rev. Mod. Phys.* **2010**, *82*, 3045–3067.

Manuscript received: October 26, 2021
Manuscript revised: December 20, 2021
Manuscript accepted: January 6, 2022
Accepted manuscript online: January 9, 2022
Version of record online: January 29, 2022

  